LAWRENCE
LIVERMORE
NATIONAL
LABORATORY

UCRL-JRNL-216859

Formation of spinel-, hibonite-rich inclusions found in CM2 carbonaceous chrondrites

S. B. Simon, L. Grossman, I. D. Hutcheon, D. L. Phinney, P. K. Weber, S. J. Fallon

November 4, 2005

American Mineralogist, Papike volume

Disclaimer

Formation of spinel-, hibonite-rich inclusions found in CM2 carbonaceous chondrites

Steven B. Simon[1], Lawrence Grossman[1,2], Ian D. Hutcheon[3], Douglas L. Phinney[3], Peter K. Weber[3] and Stewart J. Fallon[3]

[1]Department of the Geophysical Sciences, 5734 S. Ellis Ave.

[2]The Enrico Fermi Institute, 5640 S. Ellis Ave.

The University of Chicago, Chicago, IL 60637

[3]Glenn T. Seaborg Institute

Lawrence Livermore National Laboratory

P. O. Box 808, Livermore, CA 94551

E-mail: sbs8@midway.uchicago.edu

Submitted to *American Mineralogist*, Papike volume

October 26, 2005

ABSTRACT

We report petrography, mineral chemistry, bulk chemistry, and bulk isotopic compositions of a suite of 40 spinel-rich inclusions from the Murchison (CM2) carbonaceous chondrite. Seven types of inclusions are identified based on mineralogy: spinel-hibonite-perovskite; spinel-perovskite-pyroxene; spinel-perovskite-melilite; spinel-hibonite-perovskite-melilite; spinel-hibonite; spinel-pyroxene; and spinel-melilite-

anorthite. Hibonite-bearing inclusions have Ti-poor spinel compared to the hibonite-free ones, and spinel-hibonite-perovskite inclusions have the highest average bulk TiO_2 contents (7.8 wt%). The bulk CaO/Al_2O_3 ratios of the inclusions range from 0.005-0.21, well below the solar value of 0.79. Hibonite-, spinel-rich inclusions consist of phases that are not predicted by condensation calculations to coexist; in the equilibrium sequence, hibonite is followed by melilite, which is followed by spinel. Therefore, hibonite-melilite or melilite-spinel inclusions should be dominant instead. One explanation for the "missing melilite" is that it condensed as expected but was lost due to evaporation of Mg and Ca during heating and melting of spherule precursors. If this theory were correct, melilite-poor spherules would have isotopically heavy Mg and Ca. Except for one inclusion with F_{Mg}=4.3±2.6‰/amu and another with isotopically light Ca (F_{Ca}=-3.4±2.0‰/amu), however, all the inclusions we analyzed have normal isotopic compositions within their 2σ uncertainties. Thus, we found no evidence for significant mass-dependent fractionation. Our preferred explanation for the general lack of melilite among hibonite-, spinel-bearing inclusions is kinetic inhibition of melilite condensation relative to spinel. Because of similarities between the crystal structures of hibonite and spinel, it should be easier for spinel to form from hibonite than for melilite to do so.

INTRODUCTION

One way in which the origin of refractory inclusions is investigated is by comparing observed assemblages to results of equilibrium condensation calculations for a gas of solar composition. Although many refractory inclusions have undergone melting, by definition they consist of phases predicted to condense at high temperatures from a gas of solar composition. Spinel-, hibonite-bearing spherules, a major type of inclusion common in CM2 chondrites, consist of phases that are predicted by thermodynamic calculations to condense, but they are not predicted to coexist. Melilite (specifically, the gehlenite endmember, $Ca_2Al_2SiO_7$), should form by reaction between hibonite ($CaAl_{12}O_{19}$) and vapor after almost all Al is condensed into hibonite. Then, after melilite formation has consumed all the Ca remaining in the vapor, the remaining hibonite should react with the vapor to form spinel *sensu stricto*, $MgAl_2O_4$. Throughout updates and additions to the data base over the years, calculations (e.g. Grossman, 1972; Yoneda and

Grossman, 1995; Ebel and Grossman, 2000) consistently show that melilite should condense after hibonite and before spinel. Contrary to these predictions, however, spinel-free, hibonite-melilite inclusions have not been reported. Instead, hibonite-, spinel-bearing inclusions that are melilite-free or very melilite-poor are abundant among the inclusions found in CM2 chondrites, consistent with formation of spinel before melilite. For inclusions that were once molten, we assume that if melilite is present, then it was among the precursor phases that were melted. Therefore, the origin of spinel-, hibonite-rich, melilite-free inclusions has puzzled researchers for years. Some fine-grained inclusions consist of spinel-, hibonite-, perovskite nodules ± thin melilite rims, and also provide petrographic evidence for formation of spinel before melilite (Krot et al., 2004).

Explanations that have been offered in order to reconcile the observed assemblages with condensation calculations include: slower formation of melilite than spinel (MacPherson et al., 1983); preferential nucleation of spinel upon hibonite relative to melilite (Beckett and Stolper, 1994); suppression of melilite condensation due to depletion of the vapor in Al as a result of prior condensation and removal of an Al-rich phase (Beckett and Stolper, 1994); condensation under conditions of supersaturation (Petaev et al., 2005); and loss of melilite originally present, due to evaporation of Ca, Si and Mg during partial melting of the precursors (MacPherson et al., 1983). MacPherson and Davis (1994) argued that spinel would have been destabilized by evaporation of Mg during melting, but if melting occurred at a temperature at which spinel was stable, preferential evaporation of the liquid relative to spinel could enhance the evaporation rates of Si and Ca relative to Mg, possibly further stabilizing spinel. If evaporation occurred from partially molten inclusions, then they should be measurably enriched in the heavier isotopes of these elements (i.e., F_{Mg}, F_{Si}, $F_{Ca}>0$). We might also expect that melilite-free inclusions would be more fractionated than those with melilite. Previous studies of Ca (Ireland, 1990) and Mg (Ireland, 1988) isotopes in Murchison inclusions showed some positive mass-fractionations greater than analytical uncertainty and no large, negative fractionations, providing a hint that Ca and Mg evaporation did take place. That work did not reveal any correlation between Mg and Ca isotopic compositions, or between isotopic and chemical compositions. We have undertaken a petrologic and ion probe study of a variety of spinel-bearing inclusions from Murchison to see if they are

isotopically fractionated and if there are any correlations of isotopic composition with mineral assemblage. Preliminary results of this work were reported by Simon and Grossman (2004) and by Simon et al. (2005a).

ANALYTICAL METHODS

Polished sections of 40 refractory spherules and fragments thereof that were separated from the Murchison (CM2) chondrite by standard freeze-thaw techniques (e. g., MacPherson et al., 1980) were studied with a JEOL JSM-5800LV scanning electron microscope equipped with an Oxford/Link ISIS-300 energy dispersive X-ray analysis system and classified by mineral assemblage. Wavelength dispersive analyses of a subset of this suite were obtained with a Cameca SX-50 electron microprobe, operated at 15 kV and 25 nA. Pure oxide, synthetic glass, and natural mineral standards were used. Data were reduced with the modified ZAF correction procedure PAP (Pouchou and Pichoir, 1984).

Initial isotopic analyses were performed with a modified ims-3f ion microprobe at Lawrence Livermore National Laboratory (LLNL) following conventional procedures (e.g., Goswami et al., 1994; Ireland, 1990). The phases of interest in the inclusions were located by optical microscopy and ion imaging; a small field aperture inserted in the sample image plane ensured acceptance of secondary ions only from the single phase of interest. Mass-dependent isotope fractionation for Mg and Ca was determined relative to the respective compositions of appropriate terrestrial minerals. Standards included Burma spinel, Madagascar hibonite, synthetic Åk60 melilite glass, DeKalb diopside and Miakejima plagioclase. The magnitudes of isotope fractionation, F_{Mg} and F_{Ca}, were calculated as the permil/amu deviation in the respective $^{25}Mg/^{24}Mg$ and $^{44}Ca/^{40}Ca$ ratios relative to values measured in the appropriate terrestrial standards. Positive F_{Mg} and F_{Ca} values reflect compositions enriched in the heavier isotopes relative to terrestrial standards. Excesses in ^{26}Mg, from the decay of ^{26}Al, were determined using a power law mass fractionation correction; excesses are expressed as $\delta^{26}Mg$ relative to the reference $^{26}Mg/^{24}Mg$ value of 0.13932. Quoted uncertainties are two standard deviations of the

mean, and are propagated to include contributions from the reproducibility of standards and the error of individual analyses.

In a second series of analyses, Mg isotope ratios were determined with the LLNL NanoSIMS 50 ion microprobe. An $^{16}O^-$ primary beam of 10 – 30 pA focused to 0.2 – 0.3 μm diameter was rastered over selected areas of the inclusions ranging in size from 20 x 20 μm to 3 x 3 μm to generate quantitative isotope ratio images. Positive secondary ions of the three Mg isotopes and $^{27}Al^{++}$ (corresponding to mass 13.5) were measured in multi-detection mode with four different electron multipliers at a mass resolving power of ~3500 – 4000. For each area, 20 – 40 consecutive images were taken and then combined to produce an integrated 256 x 256 pixel image. The data were processed as quantitative isotopic ratio images using custom software (*L'Image*; L.R. Nittler). Each analysis area was subdivided into regions of interest (ROIs) corresponding to the different mineral phases contained in the image and the isotopic composition for each ROI calculated by integrating over all the pixels within the ROI. For each inclusion the Mg isotope compositions were normalized to the composition of spinel grains analyzed previously with the ims-3f. The Al/Mg ratios were determined using sensitivity factors generated by analyses of the terrestrial standards. The reproducibility of $^{25}Mg/^{24}Mg$ and $^{26}Mg/^{24}Mg$ ratios was within several permil. These variations are included in the errors given for F_{Mg} and $\delta^{26}Mg$.

RESULTS

Petrography

The first step in this study was a detailed, systematic petrographic classification of spinel-rich spherules. Also known as "blue spherules" (MacPherson et al., 1983) or SHIBs (Ireland, 1988), spinel-rich refractory spherules from CM chondrites actually exhibit a variety of mineral assemblages and textures and should not all be grouped together. The 40 spherules or fragments thereof selected for this study are from Murchison and range from 50 to 200 μm across. They comprise 12 spinel (sp)-hibonite (hib)-perovskite (pv) inclusions; 9 sp-pv-pyroxene (pyx); 8 sp-pv-melilite (mel); 6 sp-

hib-pv-mel; 2 sp-hib; 2 sp-pyx; and one sp-mel-anorthite. While intended to represent the range of inclusion types found in Murchison, this suite is not intended to represent their relative proportions. We are mainly interested in spinel±hibonite±melilite inclusions, and these dominate our suite. Few inclusions considered here are free of both melilite and hibonite, although sp-pyx inclusions are abundant in Murchison (MacPherson et al., 1983) and even more so in Mighei (MacPherson and Davis, 1994). We have no spinel-perovskite inclusions, although such inclusions have been reported (Macdougall, 1981). Some inclusions in our suite have rims of Fe-bearing phyllosilicate enclosed in an outer rim of aluminous diopside. Most inclusions have many rounded cavities, like those shown in MacPherson et al. (1983) and Macdougall (1981) that are commonly lined with melilite or pyroxene, but some have few cavities and may be considered compact. Some spherules have uniform distributions of phases while others have phases that are concentrated in their cores relative to their edges. Representative photomicrographs (backscattered electron images) of different types of spherules are shown in Fig. 1.

Spinel-hibonite-perovskite inclusions. These inclusions would fall into the SHIB category of Ireland (1988). Most of these samples consist of hibonite laths and anhedral perovskite enclosed in spinel. The widths of hibonite laths range from just a few μm up to ~25 μm, and their lengths are 10-50 μm. Of the 12 samples in this category, nine are complete or nearly complete spherules and three are irregularly-shaped fragments. Four spherules (e. g., Fig. 1a) have a uniform distribution of phases and four have hibonite-rich cores and spinel-rich rims (Fig. 1b). The remaining complete inclusion has an unusual structure, with a massive outer rim of spinel and a porous core of spinel + perovskite separated by a band of hibonite + perovskite. Among the three fragments of sp-hib-pv spherules, one is dominated by coarse hibonite with interstitial perovskite and spinel; one has approximately equal proportions of spinel and hibonite with minor perovskite; and one has sparse, thin hibonite laths and small, round perovskite grains enclosed in spinel.

Spinel-perovskite-pyroxene inclusions. With only one exception, these inclusions consist of fine (5-10 μm), anhedral perovskite and pyroxene (aluminous diopside) enclosed in porous or massive spinel. An example is shown in Fig. 1c. All of these inclusions have rims of Al-diopside as well. One inclusion, M98RXL-5, differs markedly from the others in this group and is shown in Fig. 1d. It is quite large (~200 × 150 μm)

and consists of lath-shaped spinel with interstitial pyroxene and perovskite. Pore space and perovskite abundances decrease and pyroxene increases from core to rim. The inclusion is enclosed in rim layers of pyroxene and olivine.

Spinel-perovskite-melilite inclusions. Six of these eight inclusions are texturally similar to the typical sp-pv-px inclusions, having fine, anhedral perovskite and melilite enclosed in cavity-riddled spinel (Fig. 1e). One sp-pv-mel inclusion has both fine and coarse (~25 μm) melilite enclosed in spinel. The remaining sp-pv-mel inclusion is dominated by melilite and resembles a fragment of a compact Type A inclusion, with coarse, euhedral spinel and fine perovskite enclosed in melilite. Only two of the sp-pv-mel inclusions have rims of pyroxene.

Spinel-hibonite-perovskite-melilite inclusions. This group exhibits the most textural diversity among the petrographic types we have distinguished. Only two spherule fragments have textures that are similar to each other. One is shown in Fig. 1f. They are dominated by spinel and hibonite with fine, anhedral inclusions of melilite and perovskite. One spherule fragment, M92H2-5 (Fig. 1g), is zoned, with a spinel-hibonite-perovskite mantle enclosing a melilite-spinel core. Another, M98L4 (Fig. 1h) is unusual in having relatively abundant and coarse melilite occurring interstitial to hibonite laths and enclosed in spinel. Two sp-hib-pv-mel inclusions included in this study, BB-1 and MUM-1, were first described by MacPherson et al. (1983). The former is an unrimmed, spherical object 100 μm across. The outer ~25 μm consist of spinel with interstitial melilite and perovskite. The interior is dominated by hibonite with finer, anhedral melilite, perovskite and spinel. The melilite in this inclusion is in contact with either hibonite or cavities. Inclusion MUM-1 is an unusual (for a CM chondrite), melilite-dominated inclusion. A chain of subhedral spinel crystals runs through the inclusion, and most of the hibonite is enclosed in spinel. Along one edge of the inclusion fragment is a rim sequence of, from inside to outside, spinel, melilite, anorthite, and diopside.

Spinel-hibonite inclusions. One of these samples, SH-6, was previously shown and described by MacPherson et al. (1984). The other sample, SH-5, is texturally similar to SH-6. Both samples are structurally zoned, with interiors consisting of fluffy aggregates of hibonite laths 5-10 μm long partially enclosed by an outer zone of

relatively massive spinel. At the spinel-hibonite contact, spinel has a lathlike morphology similar to that of the hibonite.

Spinel-pyroxene inclusions. These two samples consist of porous spinel with small (<10 μm), anhedral inclusions of pyroxene, in a texture similar to that of typical sp-pv-pyx spherules (Fig. 1c). Both of the sp-pyx spherules are rimmed by pyroxene.

Spinel-melilite-anorthite inclusion. One unrimmed spherule consists almost completely of spinel, with sparse, small (<10 μm) inclusions of anhedral melilite and anorthite.

Mineral chemistry

In all inclusions considered here, spinel is very close to endmember $MgAl_2O_4$ in composition, with small Ti, V, Cr and Fe oxide components. Contents of V_2O_3 and TiO_2 in spinel in the four most abundant inclusion types are summarized in Fig. 2. Within each plot, each symbol (e.g., filled triangles) represents data from one inclusion. For most inclusions, the analyses tend to form tight clusters on these plots, although the spinel in several of the sp-pv-px inclusions (Fig. 2a) exhibits fairly wide ranges of TiO_2 contents. Except for the sp-hib-pv-mel inclusions (Fig. 2d), the groups shown have bimodal distributions of V_2O_3 contents. In the sp-pv-px inclusions, there is a gap from ~0.15-0.25 wt% V_2O_3; among sp-hib-pv inclusions (Fig. 2b), spinel from a given inclusion has either <0.2 wt% V_2O_3 or >0.2 wt% V_2O_3; and, among sp-pv-mel inclusions (Fig. 2c), there is a gap from ~0.2-0.34 wt% V_2O_3, and only one inclusion has spinel with V_2O_3 contents between 0.2 and 0.55 wt%; unlike the other types, several of these inclusions contain spinel with >0.55 wt% V_2O_3. Spinel in the two melilite-rich inclusions, MUM-4 and MUM-1 (open triangles in Figs. 2c and d, respectively), is the most V_2O_3-rich among the present samples, but it is not as V-rich as spinel in fluffy Type A inclusions, which typically contains >1.5 wt% V_2O_3 (MacPherson and Grossman, 1984). Figure 2 also shows that spinel with >0.5 wt% TiO_2 is more common in pyroxene-bearing inclusions than in the other inclusion types.

Hibonite compositions are summarized in Fig. 3 and representative analyses are given in Table 1. Hibonite exhibits a range of Ti and Mg contents, which are strongly correlated, as Ti^{4+} (and Si^{4+}) enters hibonite along with Mg in a coupled substitution for

two Al^{3+} cations. We assume that the small amounts of FeO in some of the analyses are due to secondary substitution for Mg, so we plot Mg + Fe *vs.* Ti + Si in Fig. 3, and the line for which Ti + Si = Mg + Fe is shown for reference. In these samples the TiO_2 content of hibonite ranges from 1.1 to 9.0 wt%. There is much overlap between the sp-hib-pv and the sp-hib-pv-mel inclusions, with the former exhibiting a slightly wider range of Ti and Mg contents than the latter. The analyses, especially those at the high Ti + Si end of the trend, that plot below the Ti + Si = Mg + Fe line probably reflect the presence of a small Ti^{3+} component, which can substitute for Al directly and therefore is not coupled with Mg.

The average V_2O_3 and TiO_2 contents of coexisting hibonite and spinel are compared in Fig. 4. There is a strong positive correlation between the average V_2O_3 content of hibonite in a given inclusion and that of spinel in the same inclusion (Fig. 4a). In contrast, no such correlation is observed for the TiO_2 contents of these coexisting phases (Fig. 4b). The different systematics probably reflect different partitioning behavior, as discussed below. The sample that has V-rich hibonite and plots off the trend in Fig. 4a is fragment of an otherwise typical sp-hib-pv inclusion. The sample with Ti-rich spinel, plotting at ~0.98 wt% TiO_2 in Fig. 4b, is the unusual, fluffy sp-hib inclusion SH-6.

Melilite compositions are plotted in Fig. 5, which shows that all melilite in the inclusions analyzed for this study has ≤ 0.05 wt% Na_2O and, with the exception of MUM-4, is more aluminous than $Åk_{15}$. In MUM-4 the melilite is $Åk_{20\text{-}30}$. There is no correlation between Na_2O and åkermanite contents. The Al-rich melilite compositions of the melilite-rich inclusions are like those of the fluffy Type A inclusions found in CV3 chondrites (MacPherson and Grossman, 1984) but the textures of the Murchison inclusions are more compact. Like that in MUM-4, most melilite in compact Type A inclusions is $Åk_{20\text{-}30}$ but, unlike that in MUM-4, most spinel in the compact Type As has <0.8 wt% V_2O_3 (Simon et al., 1999). To complete the comparison, in Type B coarse-grained inclusions, also found in CV3 chondrites, spinel typically has 0.2 – 0.9 wt% V_2O_3 (Connolly et al., 2003) and melilite that is mostly $Åk_{>25}$ (Simon and Grossman, in press).

Pyroxene in the spherules is Mg-, Ca-rich clinopyroxene with a wide range of Al_2O_3 and TiO_2 contents. Representative analyses are given in Table 2. Unlike the Ti-rich

pyroxene in coarse-grained inclusions, termed “fassaite” by Dowty and Clark (1973), the pyroxene in the spherules is very poor in Sc_2O_3 and V_2O_3. For example, most Sc_2O_3 contents are below the detection limit of the electron probe and all are <0.06 wt%. This is lower than the Sc_2O_3 contents of most of the fassaite in compact Type A (Simon et al., 1999) and Type B (Simon et al. 1991) inclusions in CV3 chondrites, which reach ~2 and ~1 wt%, respectively. Pyroxene V_2O_3 contents are more like those of coarse-grained inclusions and are mostly between 0.1 and 0.5 wt%. Contents of Al_2O_3 in spherule pyroxenes are plotted against TiO_2^{tot} (all Ti reported as TiO_2) contents in Fig. 6. Almost all pyroxene in the rims of inclusions has < 2 wt% TiO_2^{tot} and is Al-poor compared to that in the interiors of inclusions. Most pyroxene in the interiors of inclusions is Al-rich, has > 5 wt% TiO_2^{tot} and Ti^{3+}/Ti^{tot} from 0.16-0.65 (mostly between 0.2 and 0.4), calculated according to the methods of Beckett (1986). This contrast indicates that, even though most of the pyroxene in the interiors of inclusions fills interstices, it is not simply rim material that penetrated into the inclusions

In one spinel-perovskite-pyroxene inclusion we found a small (~3 μm), rounded, Ca-free oxide grain. It is enclosed in spinel and contains about 17 wt% MgO, 19% Al_2O_3 and 64% TiO_2, corresponding to a formula approaching $Mg_2Al_2Ti_4O_{13}$.

Spherule Bulk Chemical Compositions

From the phase volume proportions and their densities, weight proportions of the phases in a subset of spherules were determined and, along with average phase compositions, were used to calculate inclusion bulk compositions. Neither phases in rim layers nor secondary alteration products were included in the modes. For this work we selected rim-to-rim sections of spherules or fragments that appear to be from homogenous inclusions. For concentrically zoned spherules, compositions of cores and mantles were calculated separately, then combined according to their weight proportions. We avoided inclusion fragments with heterogeneous distributions of phases, but otherwise the inclusions are small enough (~100 μm across) that we can assume that the sections sample them representatively. Average compositions of each group are listed in Table 3. The inclusions are all dominated by spinel and thus are rich in Al_2O_3 (all have

>50 wt%) and MgO (all >15 wt%). The spinel-hibonite-perovskite inclusions can be quite perovskite-rich, and as a result this group has the highest average TiO_2 as well as the lowest SiO_2 contents. The CaO/Al_2O_3 ratios of the inclusions range from 0.0045 to 0.21, much lower than the solar value of 0.79.

The spherule bulk compositions plot well off trajectories of bulk equilibrium condensate compositions, such as the one calculated for a solar gas at $P^{tot} = 10^{-3}$ bar shown in Fig. 7, a plot of MgO vs. Al_2O_3 contents. Compositions of phases and their endmember components are also plotted. Compositions of inclusions that are dominated by two phases, such as sp-pv-pyx inclusions that have only minor perovskite, fall along mixing lines between their major phases. The inclusion compositions do not appear to have been displaced from those of condensates by addition of spinel to condensate assemblages. Mathematical subtraction of spinel from the compositions to yield the solar CaO/Al_2O_3 ratio, using the method of Grossman et al. (2000), in many cases yields unrealistic compositions that have negative MgO contents and/or >30 wt% TiO_2.

We also tried a calculation in which a sufficient amount of gehlenite was added to each spherule composition to increase its CaO/Al_2O_3 ratio to the solar value. As Fig. 7 shows, these "corrected" compositions plot on or close to the condensate trajectory. The scatter in the data is greatly reduced, and the compositions plot much closer to the condensate trajectory, compared to the raw data, on all oxide-oxide plots even though melilite is not present in all of the inclusions. Large proportions of melilite, ~4g mel per gram of inclusion, are needed. As a result, after renormalization the melilite-corrected compositions of the spherules are similar to compositions of compact Type A (very melilite-rich) inclusions that have been corrected to the solar CaO/Al_2O_3 ratio by melilite subtraction, which for these inclusions is analogous to addition of spinel (Grossman et al., 2000). Corrected Type A compositions are also shown in Fig. 7. They have slightly lower Al_2O_3 and CaO and higher MgO contents than the corrected spherule compositions.

Spherule Bulk Isotopic Compositions

Isotopic compositions of a small suite of inclusions were determined by ion microprobe. The inclusions are small enough that we assume that the analyses are

representative of the bulk compositions. Results are summarized in Table 4 and Fig. 8. Data for samples with both F_{Mg} and F_{Ca} available are plotted in Fig. 8a. Where only F_{Mg} is available, the data are plotted in Fig. 8b. In most cases, our 2σ uncertainties are <50% of the uncertainty of 5‰/amu obtained for F_{Mg} and for F_{Ca} by Ireland (1988; 1990). Within each inclusion, coexisting phases have uniform F_{Mg} and F_{Ca} values. If the spherules underwent evaporation while partially molten in the solar nebula, the isotopic compositions of Mg and Ca should be strongly fractionated in favor of the heavy isotopes. This is not observed in our results for either Mg or Ca. Except for one inclusion, BB-1, that is weakly to moderately fractionated (F_{Mg}=4.3±2.6 ‰/amu), only small mass-fractionation effects are seen, with F_{Mg} within error of 0 for the other nine inclusions analyzed. MacPherson and Davis (1994), in their study of refractory inclusions from Mighei, also found low F_{Mg} values for spinel-rich objects. We found F_{Ca} to be within error of 0 for four of five inclusions analyzed. The sample with F_{Ca} that is not within analytical uncertainty of 0‰/amu is M92H2-34; its F_{Ca}=-3.4±2.0‰/amu, so its Ca isotopic composition is light.

In addition, we investigated Mg-Al systematics in six inclusions. Refractory inclusions commonly contained live ^{26}Al, a short-lived radionuclide that decays to ^{26}Mg with a half-life of 7.3×10^5 yr, when they formed. In a sample that initially contained live ^{26}Al, δ^{26}Mg will now be positively correlated with Al/Mg. Our results are given in Table 5 and illustrated in Fig. 9. We found that three sp-hib-pv-mel inclusions (M98L4, MUM-1 and BB-1) and two sp-hib-pv inclusions (M98M11, M92H2-34) have measurable excesses of ^{26}Mg correlated with Al/Mg, yielding initial ^{26}Al/^{27}Al ratios within error of 5×10^{-5}, as illustrated in Fig. 9. This is a common initial ratio among refractory inclusions (MacPherson et al., 1995). In contrast, one sp-hib-pv-mel inclusion (M92H2-5, shown in Fig. 1g) has a very low initial ratio, $<3.6\times10^{-6}$. Except for MUM-1, these inclusions could be classified as SHIBs according to the scheme of Ireland (1988), and this type of inclusion commonly contains radiogenic ^{26}Mg (Ireland, 1988; 1990), as do most melilite-bearing, coarse-grained inclusions from CV chondrites (MacPherson et al., 1995; Simon et al., 2001). It is therefore unusual to find a melilite-bearing inclusion (M92H2-5) that did not contain live ^{26}Al when it formed.

DISCUSSION

Significance of Petrographic Groupings

Some of the inclusions contain very small amounts of one or more of the phases used to classify them. If they were all assembled from the same suite of precursor grains, and if the various petrographic types of inclusions that we distinguished merely reflect nonrepresentative sampling in the laboratory rather than genetic differences, there should be few systematic mineral-chemical differences related to the petrographic groupings. The spinel in one type of inclusion would be no different from that in any other type, and the plots in Fig. 2 would all look very similar to each other. Although there is some overlap in compositions among spinel from different types of inclusions, there are, as shown in Fig. 2, also differences between types. For example, spinel in most of the sp-pv-px inclusions, unlike that in other types, has wide ranges of TiO_2 contents. Several sp-pv-mel inclusions have spinel with higher V_2O_3 contents than spinel in any of the sp-pv-px inclusions we analyzed. In addition, the correlation of V_2O_3 contents in coexisting hibonite and spinel (Fig. 4a) and the homogeneity of isotopic compositions of coexisting phases suggest that, within each spherule, the phases are related to each other and do not represent random assemblages of grains that have been sampled with various degrees of accuracy.

Generation of Observed Mineral Assemblages and the "Missing Melilite"

Many of the inclusions upon which this study is based have features, such as interlocking spinel and hibonite grains, and hibonite laths that interfered with each other during growth, that suggest that they crystallized from molten droplets. In addition, the correlated V and uncorrelated Ti contents of coexisting spinel and hibonite (Fig. 4) are also consistent with igneous histories for the samples. Experiments have shown that V_2O_3 is compatible in spinel during crystallization from a melt, especially at low oxygen fugacities (Connolly and Burnett, 2003). Thus, if V is also compatible in hibonite, it is reasonable that V contents in hibonite and spinel would be correlated with each other

and, therefore, with bulk V_2O_3 contents of the host spherules. On the other hand, TiO_2 is strongly incompatible in spinel (Connolly and Burnett, 2003). The partitioning behavior of TiO_2 in hibonite ranges from weakly incompatible to strongly compatible, and the crystal/liquid partition coefficient decreases with increasing bulk TiO_2 content (Beckett and Stolper, 1994). This leads to weak relationships between hibonite and bulk TiO_2 contents and between spinel and hibonite TiO_2 contents. The contrasting systematics observed for V and Ti in coexisting spinel and hibonite are thus consistent with their different partitioning behavior with respect to these phases, showing that the spinel and hibonite within most inclusions is genetically related to each other. It is therefore not surprising that the anomalous sample in the Ti plot (Fig. 4b) is SH-6, which is likely a gas-solid condensate that was never molten (MacPherson et al., 1984). The sample with V-rich hibonite, that plots off the V trend in Fig. 4a, probably is either also a condensate, or contains relict hibonite.

At the temperatures required to keep these objects even partially molten, which are >2000 °C for their present bulk compositions, Mg, Si and even Ca should volatilize in a reducing gas. Our analyses, however, yield values of F_{Mg} that are lower than those typical of Type B CAIs (Grossman et al., 2000), implying smaller mass losses than in the case of those inclusions. In addition, our calculations show that to correct the spherule bulk compositions to the solar CaO/Al_2O_3 ratio requires adding so much melilite that they approach the compositions of Type A inclusions, which MacPherson et al. (1983) suggested as a possible precursor condensate assemblage. To derive the compositions of the spherules we studied through evaporation from such equilibrium condensates would require losses of 75-95% of the Ca originally present, which would lead to F_{Ca} values on the order of 17-35‰/amu. This is neither observed here nor in any previous studies. If Ca were not lost, then evaporation is not the reason for the low melilite contents of hibonite-, spinel-rich inclusions. Given that most of the inclusions were once molten, the lack of evidence for evaporation is puzzling. Perhaps evaporation rates were so high that, analogous to distribution coefficients in a rapidly cooling melt, evaporation coefficients approached unity, leading to mass fractionations that are presently undetectable.

If evaporation did not occur, however, there must be another explanation for the “missing melilite”, and several have been offered by various workers. Most are

problematic. One suggestion that is unsatisfactory is that condensation of a highly aluminous phase removed enough Al (~20%) to delay melilite formation relative to spinel (Beckett and Stolper, 1994). This will not work, because all Al must be condensed into hibonite before either melilite or spinel becomes stable, and hibonite is needed to react with the gas to make melilite and spinel. Furthermore, the present samples and fine-grained, hibonite-, spinel-bearing inclusions have very low Ca/Al ratios relative to a solar gas, which would not be expected for formation from an Al-depleted source. The only way to delay gehlenite condensation relative to spinel would be to remove Ca from the gas in a refractory phase without removing Mg. Removal of early, Al-rich condensates would not lead to condensation of melilite before spinel.

It has also been suggested (Petaev et al., 2005) that a combination of a) condensation at low pressure ($<\sim 2.5 \times 10^{-4}$ bar) under conditions that are far from equilibrium, with rapid cooling of the gas; and b) incomplete condensation of all minerals that should condense before spinel, including melilite, would lead to condensation of spinel before melilite. There is no direct evidence for this process, and there is no apparent reason why spinel should condense completely when all phases preceding it did not. Petaev et al. (2005) suggest that if the Al-diopside found enclosing spinel-rich nodules in fine-grained CAIs (Krot et al., 2004) is a condensate, it would require that hibonite stop condensing before it consumed all the gaseous Al and that some Al remained in the gas even after the formation of aluminates, melilite and spinel. For this to occur is very far from the predictions of models of equilibrium condensation (e.g., Yoneda and Grossman, 1995), and we find it highly unlikely.

Rare spinel-hibonite inclusions have been found in Murchison that appear to record formation of spinel directly from hibonite. An example is shown in Fig. 10. This sample, SH-6, is a fluffy aggregate of hibonite plates with a rind of spinel. It was first described by MacPherson et al. (1984), who presented very strong arguments that this object is a condensate. As pointed out by MacPherson et al. (1984), the interior of this inclusion, visible in the left half of Fig. 10, is monomineralic, with euhedral hibonite crystals and a high volume of void space, features that are not consistent with crystallization from a melt, but are consistent with vapor-solid condensation. In addition, some of the spinel grains have a lathlike morphology like that of hibonite. This

morphology is very unusual for spinel, and was almost certainly inherited from precursor grains of hibonite. As noted by MacPherson et al. (1984), at the hibonite-spinel contact, there are laths that consist of hibonite at one end and spinel at the other. Several of these are indicated by arrows in Fig. 10. Formation of spinel from hibonite appears to have gone to completion in Murchison inclusion M98RXL-5 (Fig. 1d), which consists of spinel laths and interstitial clinopyroxene. It looks like a fluffy hibonite aggregate but contains no hibonite at all.

There are no known samples that are melilite analogs of M98RXL-5, i.e., dominated by melilite pseudomorphs after hibonite. Simon et al. (2005b), however, have recently described two inclusions from an Antarctic CM2, LEW85311, that exhibit partial replacement of hibonite by melilite. An example is shown in Fig. 11, which consists of a backscattered electron image (11a), and Al, Si and Ca X-ray maps (Fig. 11b-d, respectively). Note the hibonite grain, indicated by an arrow, that has been converted to melilite along its upper edge (as seen in this view), where the grain is in contact with a cavity. Nearby, hibonite contains thin, Si-, Ca-bearing bands that occur along cleavage traces and grain boundaries. These can be seen in the X-ray maps within the outlined area. Analyses of these blades and of other, diffuse SiO_2-bearing areas within hibonite fall on mixing lines between hibonite and melilite, consistent with finely intergrown mixtures of the two phases. Melilite can follow hibonite in the crystallization sequences of some liquids, but that normally leads to sharp grain boundaries. What we see in this sample, with diffuse hibonite-melilite contacts and melilite occurring adjacent to void space and along cleavage traces, appears consistent with infiltration of the nebular vapor into the inclusion and reaction between hibonite and gas, forming melilite. This inclusion could be a condensate that became rounded by abrasion with other particles. Although there are some inclusions, such as the one in Fig. 11, that appear to record incipient conversion of hibonite to melilite, the extent of this reaction appears to have been much more limited than that of the spinel-forming reaction among the refractory inclusions in CM2 chondrites.

The textures of the inclusions shown in Figs. 10 and 11 reflect the fact that neither spinel nor melilite can simply condense from the nebular vapor onto hibonite; both spinel and melilite must form by reaction between solid hibonite and the surrounding gas,

because aluminum must be completely condensed for either melilite or spinel to be stable (Yoneda and Grossman, 1995). Lower temperatures are required for pyroxene formation than for melilite or spinel formation, and it is much more likely that the Al-diopside found in the fine-grained inclusions, like the spinel in the inclusion shown in Fig. 10, formed by reaction between Al-poor gas and Al-rich solids, than it is that a significant amount of Al remained in the gas *after* formation of hibonite, spinel and melilite (Petaev et al., 2005).

This leaves kinetic suppression of melilite condensation relative to spinel, first suggested by Bar-Matthews et al. (1982), as the most likely explanation for the general lack of melilite in hibonite-bearing, spinel-rich inclusions. Why might formation of spinel from hibonite have been favored over melilite formation? Comparison of the crystal structures provides a possible explanation. As noted by Beckett and Stolper (1994), there are similarities between the hibonite structure and that of spinel that could promote formation of spinel rather than melilite. The hibonite structure has Al-oxide layers and Ca-bearing layers. The former, called "spinel slabs" (Wagner and O'Keeffe, 1988) or "spinel blocks" (Burns and Burns, 1984), have sheets of Al-centered, edge-sharing octahedra, as does spinel. These structures are illustrated in Fig. 12. The composition of the spinel slab within the hibonite structure is $(Al_{11}O_{16})^{+}$ (Wagner and O'Keeffe, 1988), and Beckett and Stolper (1994) suggested that spinel would readily nucleate on such a substrate. In contrast, the Ca-bearing layers in hibonite are not analogous to any part of the melilite structure. Calcium is 12-coordinated in hibonite and is 8-coordinated in melilite. It should therefore be much easier for spinel to form from hibonite than for melilite to form from hibonite. We therefore favor, as did MacPherson and Davis (1994), kinetic inhibition of melilite formation, relative to spinel formation, as the best explanation for the origin and high abundance of spinel-, hibonite-rich, melilite-poor inclusions, relative to melilite-rich ones, in the CM2 chondrites. Some condensate assemblages were at least partially melted, forming spherules. There were, of course, some regions of the nebula where physico-chemical conditions were such than melilite did form in proportions relative to spinel that are much closer to the predictions of equilibrium condensation calculations, giving rise to the Types A and B refractory inclusions. Some Type A inclusions appear to be gas-solid condensates (MacPherson and

Grossman, 1984; Simon et al., 1999), while the Type Bs have crystallized from partial melts of solid precursors (Stolper and Paque, 1986). The melilite-rich inclusions were incorporated into the CV and CO carbonaceous chondrites, and the melilite-poor inclusions were incorporated into the CMs.

ACKNOWLEDGMENTS

The first author thanks Jim Papike for giving him his start in professional research and for his unwavering support ever since. This work was supported by NASA through grants NAG-11588 and NNG05GG00G (LG) and NNH04AB47I (IDH), and funding is gratefully acknowledged. Part of this work was performed under the auspices of the U. S. Dept. of Energy by the University of California, Lawrence Livermore National Laboratory under Contract No. W-7405-Eng-48.

REFERENCES CITED

Anders, E. and Grevesse N. (1989) Abundances of the elements: Meteoritic and solar. Geochimica et Cosmochimica Acta, 53, 197-214.

Bar-Matthews, M., Hutcheon, I.D., MacPherson, G.J., and Grossman, L. (1982) A corundum-rich inclusion in the Murchison carbonaceous chondrite. Geochimica et Cosmochimica Acta, 46, 31-41.

Beckett, J.R. (1986) The origin of calcium, -aluminum-rich inclusions from carbonaceous chondrites: an experimental study. Ph. D. dissertation, University of Chicago, Chicago, Illinois.

Beckett, J.R. and Stolper, E. (1994) The stability of hibonite, melilite and other aluminous phases in silicate melts: Implications for the origin of hibonite-bearing inclusions from carbonaceous chondrites. Meteoritics, 29, 41-65.

Burns, R.G. and Burns, V.M. (1984) Crystal chemistry of meteoritic hibonites. Proceedings of the 15th Lunar and Planetary Science Conference, Journal of Geophysical Research, 89, supplement, C313-C321.

Connolly, H.C. Jr. and Burnett, D.S. (2003) On type B CAI formation: Experimental constraints on f_{O2} variations in spinel and minor element partitioning and re-equilibration effects. Geochimica et Cosmochimica Acta, 67, 4429-4434.

Connolly, H.C. Jr., Burnett, D.S., and McKeegan, K.D. (2003) The petrogenesis of type B1 Ca-Al-rich inclusions: The spinel perspective. Meteoritics & Planetary Science, 38, 197-224.

Dowty, E. and Clark, J.R. (1973) Crystal structure refinement and optical properties of a Ti^{3+} fassaite from the Allende meteorite. American Mineralogist 58, 230-242.

Ebel, D.S. and Grossman, L. (2000) Condensation in dust-enriched systems. Geochimica et Cosmochimica Acta, 64, 339-366.

Goswami J.N., Srinivasan, G., and Ulyanov, A.A. (1994) Ion microprobe studies of Efremovka CAIs: I. Magnesium isotope composition. Geochimica et Cosmochimica Acta, 58, 431-447.

Grossman, L. (1972) Condensation in the primitive solar nebula. Geochimica et Cosmochimica Acta, 36, 597-619.

Grossman, L., Ebel, D.S., Simon, S.B., Davis, A.M., Richter, F.M., and Parsad, N.M. (2000) Major element chemical and isotopic compositions of refractory inclusions in C3 chondrites: The separate roles of condensation and evaporation. Geochimica et Cosmochimica Acta, 64, 2879-2894.

Ireland, T.R. (1988) Correlated morphological, chemical, and isotopic characteristics of hibonites from the Murchison carbonaceous chondrite. Geochimica et Cosmochimica Acta, 52, 2827-2839.

Ireland, T.R. (1990) Presolar isotopic and chemical signatures in hibonite-bearing refractory inclusions from the Murchison carbonaceous chondrite. Geochimica et Cosmochimica Acta, 54, 3219-3237.

Krot, A.N., MacPherson, G.J., Ulyanov A.A., and Petaev, M.I. (2004) Fine-grained, spinel-rich inclusions from the reduced CV chondrites Efremovka and Leoville: I. Mineralogy, petrology, and bulk chemistry. Meteoritics & Planetary Science, 39, 1517-1553.

Macdougall, J.D. (1981) Refractory spherules in the Murchison meteorite: Are they chondrules? Geophysical Research Letters, 8, 966-969.

MacPherson, G.J. and Davis, A.M. (1994) Refractory inclusions in the prototypical CM chondrite, Mighei. Geochimica et Cosmochimica Acta, 58, 5599-5625.

MacPherson, G.J. and Grossman, L. (1984) “Fluffy” type A Ca-, Al-rich inclusions in the Allende meteorite. Geochimica et Cosmochimica Acta, 48, 29-46.

MacPherson, G.J., Bar-Matthews, M., Tanaka, T., Olsen E., and Grossman, L. (1980) Refractory inclusions in Murchison: recovery and mineralogical description (abstract). Lunar and Planetary Science XI, 660-662. Lunar and Planetary Institute, Houston, TX.

MacPherson, G.J., Bar-Matthews, M., Tanaka, T. Olsen, E., and Grossman, L. (1983) Refractory inclusions in the Murchison meteorite. Geochimica et Cosmochimica Acta, 47, 823-839.

MacPherson, G.J., Grossman, L., Hashimoto, A., Bar-Matthews, M., and Tanaka, T. (1984) Petrographic studies of refractory inclusions from the Murchison meteorite. Proceedings of the 15th Lunar and Planetary Science Conference, Journal of Geophysical Research, 89, supplement, C299-C312.

MacPherson, G.J., Davis, A.M., and Zinner, E,K. (1995) The distribution of aluminum-26 in the early solar system- A reappraisal. Meteoritics, 30, 365-386.

Petaev, M.I., Krot, A.N., and Wood, J.A. (2005) Nebular condensation under incomplete equilibrium: Implications for the fine-grained spinel-rich CAIs (abstract). Lunar and Planetary Science XXXVI, #1238 (CD-ROM). Lunar and Planetary Institute, Houston, TX.

Pouchou, J.L. and Pichoir, F. (1984) A new model for quantitative x-ray microanalysis. Part I: Application to the analysis of homogeneous samples. La Recherche Aerospatiale, 1984-3, 13-38.

Simon, S.B. and Grossman, L. (2004) Spinel-rich spherules from Murchison: A review and some questions (abstract). Workshop on Chondrites and the Protoplanetary Disk, 185-186. Lunar and Planetary Institute, Houston, TX.

Simon, S.B., Grossman, L., and Davis, A.M. (1991) Fassaite composition trends during crystallization of Allende Type B refractory inclusion melts. Geochimica et Cosmochimica Acta, 55, 2635-2655.

Simon, S.B., Davis, A.M., and Grossman, L. (1999) Origin of compact type A refractory inclusions from CV3 carbonaceous chondrites. Geochimica et Cosmochimica Acta, 63, 1233-1248.

Simon, S.B., Davis, A.M., and Grossman, L. (2001) Formation of orange hibonite, as inferred from some Allende inclusions. Meteoritics & Planetary Science, 36, 331-350.

Simon, S.B., Grossman, L., Hutcheon, I.D., and Phinney D.L. (2005a) Bulk chemical and isotopic compositions of spinel-, hibonite-rich spherules: Clues to their origin (abstract). Lunar and Planetary Science XXXVI, #2211 (CD-ROM). The Lunar and Planetary Institute, Houston, TX.

Simon, S.B., Keaton, C.G. and Grossman, L. (2005b) Refractory inclusions from the CM2 chondrite LEW85311 (abstract). Meteoritics & Planetary Science, 40, A141.

Stolper, E. and Paque, J.M. (1986) Crystallization sequences of Ca-Al-rich inclusions from Allende: The effects of cooling rate and maximum temperature. Geochimica et Cosmochimica Acta, 50, 1785-1806.

Tanaka, T., Davis, A.M., Hutcheon, I.D., Bar-Matthews, M., Olsen, E., MacPherson, G.J., and Grossman, L. (1980) Refractory inclusions in Murchison: Chemistry and Mg isotopic composition (abstract). Lunar and Planetary Science XI, 1122-1124. The Lunar and Planetary Institute, Houston, TX.

Wagner, T.R. and O'Keeffe, M. (1988) Bond lengths and valences in aluminates with the magnetoplumbate and β-alumina structures. Journal of Solid State Chemistry, 73, 211-216.

Waychunas, G.A. (1991) Crystal chemistry of oxides and oxyhydroxides. In D.H. Lindsley, Ed., Oxide minerals: petrologic and magnetic significance, p. 11-68, Reviews in Mineralogy, 25, Mineralogical Society of America, Washington, D.C.

Yoneda, S. and Grossman, L. (1995) Condensation of CaO-MgO-Al_2O_3-SiO_2 liquids from cosmic gases. Geochimica et Cosmochimica Acta, 59, 3413-3444.

Table 1. Representative analyses of hibonite in Murchison inclusions (wt%).

	1.	2.	3.	4.	5.
MgO	1.52	1.90	2.99	3.99	4.22
Al_2O_3	86.55	85.87	82.13	79.60	78.60
SiO_2	0.18	0.25	0.17	0.67	0.27
CaO	8.71	8.56	8.33	8.29	8.42
TiO_2	2.95	3.50	5.73	7.10	8.38
V_2O_3	0.14	0.04	0.29	0.36	0.12
FeO	0.07	0.14	0.04	BDL	BDL
Total	100.12	100.26	99.68	100.01	100.01
			Cations per 19 oxygen anions		
Mg	0.254	0.317	0.504	0.674	0.713
Al	11.428	11.327	10.964	10.620	10.506
Si	0.020	0.028	0.020	0.076	0.031
Ca	1.046	1.026	1.011	1.006	1.024
Ti	0.249	0.295	0.488	0.605	0.715
V	0.006	0.002	0.013	0.016	0.006
Fe	0.006	0.013	0.004	0	0
Total cations	13.009	13.008	13.004	12.997	12.995

1.: from a sp-hib inclusion. 2., 3.: sp-hib-pv. 4., 5.: sp-hib-pv-mel. BDL: below detection limit of electron probe (0.036 wt% FeO).

Table 2. Analyses of pyroxene in Murchison inclusions (wt%).

	1.	2.	3.*	4.*	5.*
MgO	18.46	15.89	9.96	12.87	10.68
Al_2O_3	0.53	6.92	18.23	11.94	17.85
SiO_2	55.40	50.58	39.39	42.44	36.82
CaO	25.71	25.84	24.90	24.92	23.69
TiO_2^{tot}	0.13	1.02	6.36	8.04	11.09
V_2O_3	BDL	0.06	0.15	0.28	0.42
FeO	0.10	0.25	0.56	BDL	0.04
TiO_2	-	-	3.92	5.36	8.47
Ti_2O_3	-	-	2.16	2.34	1.98
Total	100.33	100.56	99.27	100.15	99.95
		Cations per 6 oxygen anions			
Si	1.988	1.821	1.456	1.553	1.338
^{IV}Al	0.012	0.179	0.544	0.447	0.662
^{VI}Al	0.011	0.115	0.251	0.068	0.103
Mg	0.987	0.853	0.551	0.703	0.581
Ca	0.989	0.997	1.000	1.000	1.000
Ti^{4+}	0.004	0.028	0.110	0.149	0.242
Ti^{3+}	-	-	0.067	0.072	0.062
V	0	0.002	0.004	0.008	0.011
Fe	0.003	0.007	0.017	0	0.001
Total oct.	1.994	2.002	2.000	2.000	2.000

1.,2.: rim pyroxene. 3. - 5.: interior pyroxene. BDL: below limit of detection of electron probe (0.027 wt% V_2O_3 or 0.036 wt% FeO). TiO_2^{tot}: all Ti assumed to be Ti^{4+}, or TiO_2. *Ti^{3+}/Ti^{4+} ratio calculated by assuming stoichiometry and normalizing to four cations, including one Ca cation, per six oxygen anions, according to the method of Beckett (1986).

Table 3. Average compositions (and ranges) of spinel-rich inclusions from Murchison. Where greater than one, the numbers of inclusions averaged are given in parentheses in the column headings.

	Sp-Hib-Pv (7)	Sp-Hib-Pv-Mel (3)	Sp-Pv-Mel (3)	Sp-Pv-Px (8)	Sp-Mel-An	Sp-Px
MgO	20.83 (15.37-25.47)	16.51 (15.72-18.06)	26.48 (25.86-27.32)	26.01 (23.95-27.92)	28.36	27.47
Al_2O_3	64.51 (54.17-72.09)	66.00 (64.56-67.38)	67.18 (66.58-68.33)	62.72 (53.67-69.94)	70.24	67.33
SiO_2	0.49 (0.17-1.62)	3.71 (2.03-5.19)	1.04 (0.62-1.54)	4.77 (0.52-12.41)	0.57	2.50
CaO	6.41 (2.82-11.38)	9.99 (7.89-11.92)	3.18 (2.05-3.85)	3.87 (0.68-7.32)	0.32	1.68
TiO_2	7.76 (3.52-15.93)	3.79 (2.58-4.65)	2.12 (1.67-2.51)	2.61 (0.95-5.21)	0.52	1.03

Table 4. Weighted means of Mg and Ca isotopic analyses of four refractory inclusion types from Murchison (‰/amu).

	Type*	$F_{Mg} \pm 2\sigma$	$F(^{44}Ca/^{40}Ca) \pm 2\sigma$
M92H2-5	SHPvM	0.4±1.4	-0.7±2.2
M98L4	SHPvM	-0.8±1.2	0.5±2.4
BB-1	SHPvM	4.3±2.6	not measured
MUM-1	SHPvM	-1.1±2.0	not measured
M92H2-34	SHPv	1.2±1.2	-3.4±2.0
M92H2-10	SHPv	-0.6±1.4	1.4±2.4
M98M11	SHPv	3.2±5.2	-0.8±2.8
M98M18	SHPv	1.8±3.2	not measured
M98M9	SPvPx	-1.2±4.1	not measured
M92H2-37	SPx	0.8±2.2	not measured

*SHPvM: spinel-hibonite-perovskite-melilite. SHPv: spinel-hibonite-perovskite. SPvPx: spinel-perovskite-pyroxene. SPx: spinel-pyroxene.

Table 5. Ion probe measurements of $\delta^{26}Mg$ in refractory inclusions from Murchison. Abbreviations as used previously. Data for BB-1 are from Tanaka et al. (1980).

Sample	Type	Phase	$^{27}Al/^{24}Mg$	$\delta^{26}Mg$ (‰)
M92H2-34	SHPv	Hib	27± 3	12.5±5.3
M92H2-34		Hib	18±3	2±3.6
M92H2-34		Hib	14±2	9±4.8
M92H2-34		Hib	16±2	8.8±4.8
M92H2-34		Hib	15±2	6.8±4.4
M92H2-34		Hib	17±2	3.5±3.6
M92H2-34		Hib	27± 3	12.5±5.3
M92H2-34		Hib	18±3	2±3.6
M92H2-34		Sp	2.5	1.5± 2.5
M92H2-34		Sp	2.5	1.0± 2.5
M98M11	SHPv	Hib	25.7 ±3.0	19.1±3.9
M98M11		Hib	24.7 ±3	15.7±3.5
M98M11		Hib	26.7 ±4	16.1±2.8
M98M11		Hib	8.0 ±1	2.1±3.0
M98M11		Hib	13.0 ±2	8.8±3.0
M98M11		Hib	18.0 ±3	7.7±3.0
M98M11		Hib	21.0 ±2	1.7±3.3
M98M11		Hib	23.9 ±2	11.9±3.4
M98M11		Sp	2.5	0.5± 2.5
M98M11		Sp	2.5	1.6± 2.5
M98M11		Sp	2.5	0.8 ± 2.5
M98L4	SHPvM	Sp	2.5	0.5±1.5
M98L4		Hib	29.5	6.8±2.6
MUM-1	SHPvM	Sp	2.5	-0.5 ± 1.8
MUM-1		Mel	14 ± 1	2.0 ± 1.8
MUM-1		Hib	44 ± 3	13.6 ± 2.2
MUM-1		Hib	54 ± 4	19.4 ± 3.0
BB-1	SHPvM	Sp	2.5	0.3 ± 1.8
BB-1		Hib	14 ± 1	0.8 ± 2.6
BB-1		Hib	24 ± 2	5.8 ± 2.8
M92H2-5	SHPvM	Mel	17.8	2.5±3.9
M92H2-5		Sp	2.5	-1.5±1.6
M92H2-5		Hib	104.1	-0.4±3.4

FIGURE CAPTIONS

Figure 1. Backscattered electron images of spinel-rich inclusions from Murchison. a) sp-hib-pv inclusion with a uniform texture and silicate rim. b) sp-hib-pv inclusion with a hibonite-rich interior and spinel-rich mantle. c) sp-pv-px inclusion with massive spinel and small inclusions of pv and pyx. d) sp-pv-px inclusion with lath-shaped spinel that appears to pseudomorph hibonite. e) sp-pv-mel inclusion with massive spinel and blebby mel and pv. f) sp-hib-pv-mel inclusion fragment with coarse hib in the interior and a spinel-rich mantle. g) zoned sp-hib-pv-mel inclusion fragment, with a mel-rich core and sp-, hib-rich mantle. h) coarse sp-hib-pv-mel inclusion fragment. al-diop: aluminous diopside; Fe-sil: Fe-bearing silicate; Hib: hibonite; Mel: melilite; Pv: perovskite; pyx: pyroxene; Sp: spinel.

Figure 2. V_2O_3 and TiO_2 contents in spinel in the four most abundant types of inclusions considered here. Spinel in hibonite-bearing inclusions tends to have <0.5 wt% TiO_2, and melilite-bearing inclusions are more likely to contain V_2O_3-rich spinel than melilite-free ones. Abbreviations as used previously.

Figure 3. Plot of total Mg + Fe cations against total Ti + Si cations per 19 oxygen anions in hibonite from Murchison inclusions. The strong correlation reflects the dominant substitution mechanism, Mg + Ti ↔ 2Al.

Figure 4. Plots of a) average V_2O_3 in spinel *vs*. average V_2O_3 in coexisting hibonite, and b) average TiO_2 in spinel *vs.* average TiO_2 in coexisting hibonite. Each point represents one inclusion.

Figure 5. Melilite compositions in Murchison inclusions. All melilite is gehlenitic (low in the åkermanite endmember) and low in Na_2O.

Figure 6. Al_2O_3 and TiO_2^{tot} contents in pyroxene in Murchison inclusions. Pyroxene in the interiors of inclusions tends to be richer in these oxides than pyroxene in the rims of inclusions.

Figure 7. Plot of MgO *vs.* Al_2O_3 for spherule bulk compositions and compact Type A and spherule compositions "corrected" to the solar CaO/Al_2O_3 ratio of 0.792 (Anders and Grevesse, 1989), compared to a trajectory of bulk compositions of condensates from a solar gas at $P^{tot}=10^{-3}$ bar. Åk: åkermanite; CaTs: Ca-Tschermak's molecule ($CaAl_2SiO_6$); Geh: gehlenite; T3P: Ti^{3+}-bearing pyroxene component ($CaTiAlSiO_6$); T4P: Ti^{4+}-bearing pyroxene component ($CaTiAl_2O_6$). Other abbreviations as used previously.

Figure 8. Isotopic compositions of refractory inclusions, determined by ion microprobe. There is no enrichment of the heavy isotopes of Mg or Ca in these samples. Dashed lines representing 0‰ are shown for reference. a) F_{Mg} vs. F_{Ca}. b) F_{Mg} for the following samples: 1: BB-1; 2: MUM-1; 3: M98M18; 4: M98M9; 5: M92H2-37.

Figure 9. Plot showing that there is excess ^{26}Mg correlated with Al/Mg in five of six samples analyzed. The line for an initial $^{26}Al/^{27}Al$ ratio of 5×10^{-5} is shown for reference.

Figure 10. Backscattered electron image of a hibonite-bearing inclusion with clear textural evidence of direct replacement of hibonite by spinel. Examples of crystal laths that are part spinel and part hibonite are indicated by arrows. Abbreviations as used previously. Black regions are epoxy. After MacPherson et al. (1984).

Figure 11. a) Backscattered electron image, and b) – d) elemental X-ray maps, as indicated, for an area within a sp-hib-pv-mel inclusion from LEW85311, with textural evidence for formation of melilite from hibonite. Arrow indicates a hibonite grain with melilite adjacent to a cavity, and thin bands of melilite can be seen inside the area outlined by the box.

Figure 12. (left) Sketch of the “spinel slab” portion of the hibonite structure. Large circles represent Al cations; small circles, oxygen anions. The structure is dominated by edge-sharing, Al-containing octahedra, as found in the spinel structure (right).

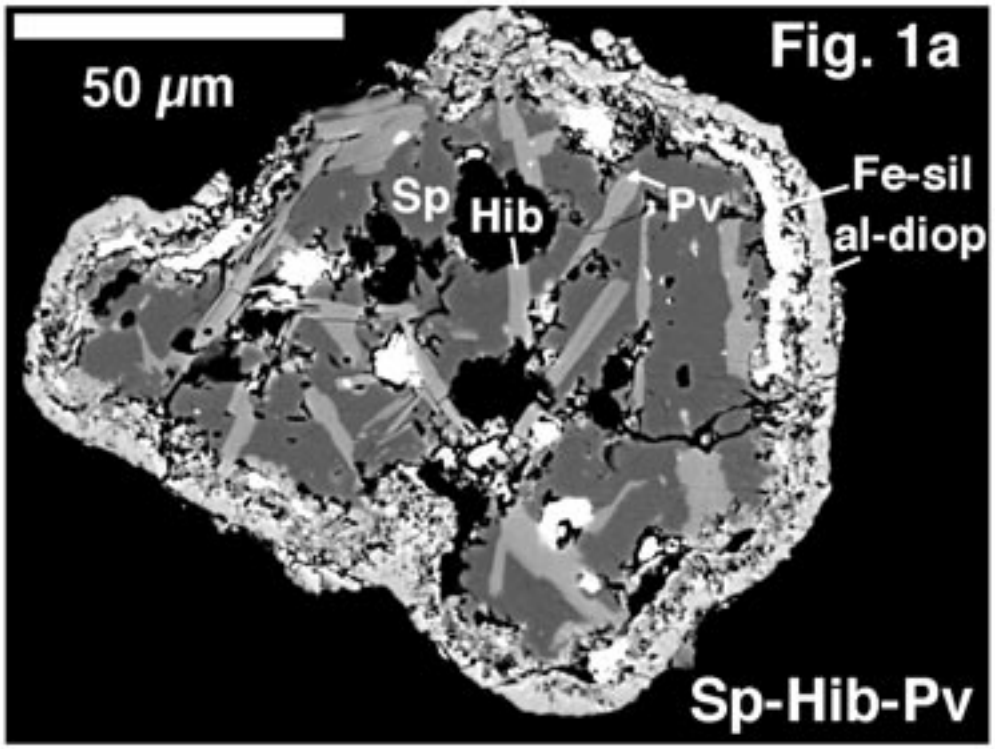
Fig. 1a
50 μm
Sp
Hib
Pv
Fe-sil
al-diop
Sp-Hib-Pv

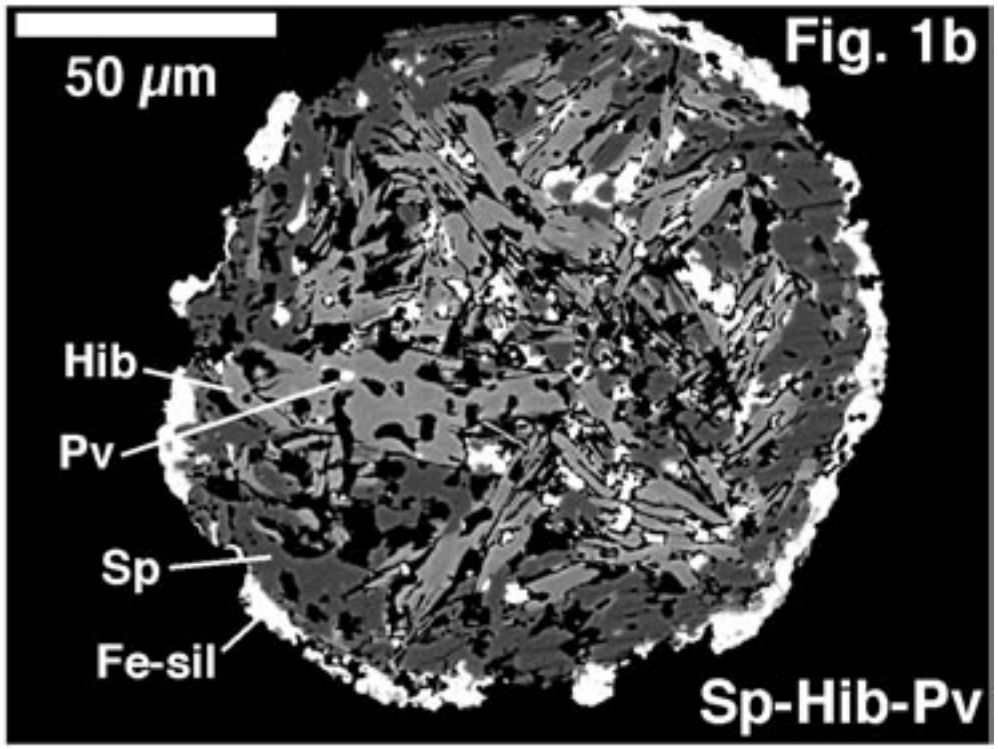
Fig. 1b
50 μm
Hib
Pv
Sp
Fe-sil
Sp-Hib-Pv

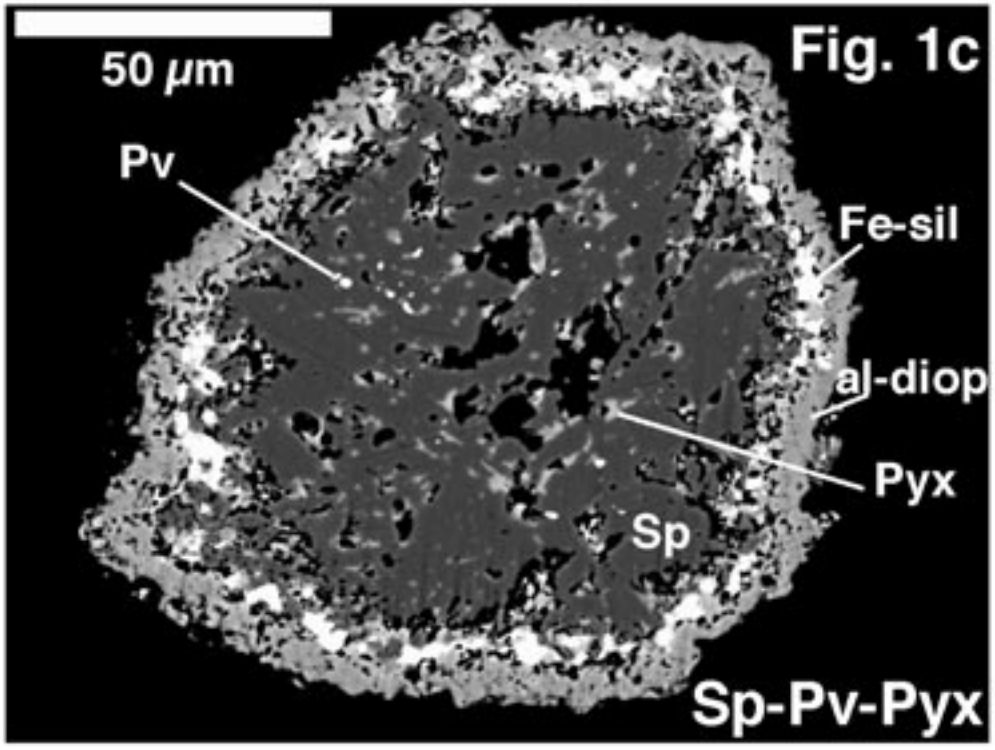
Fig. 1c
50 μm
Pv
Fe-sil
al-diop
Pyx
Sp
Sp-Pv-Pyx

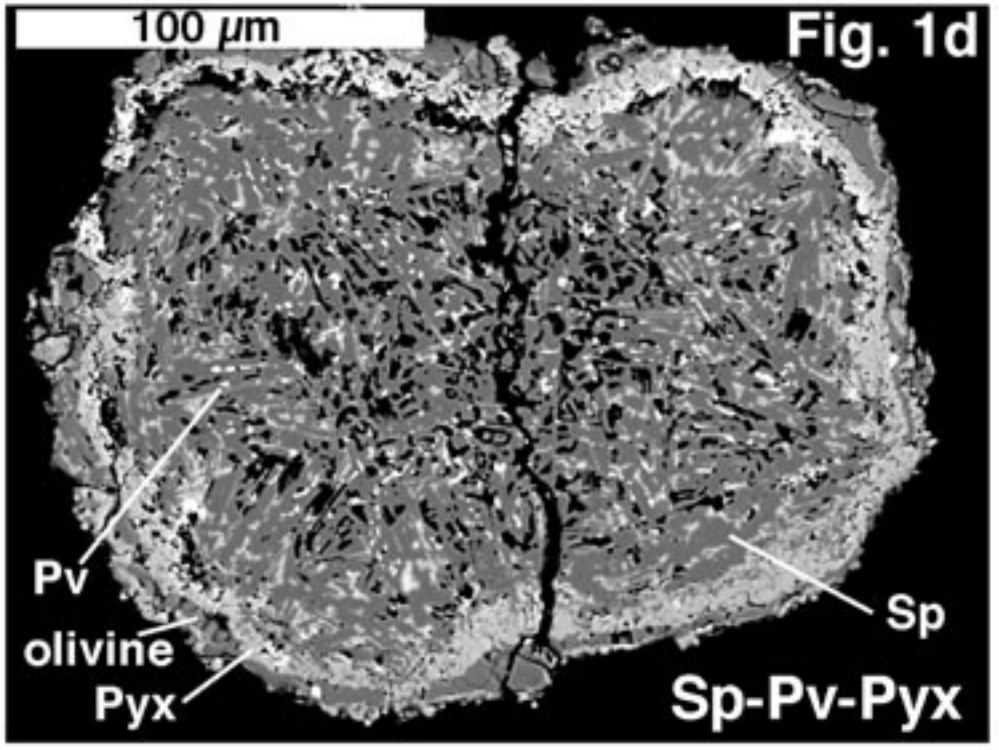
Fig. 1d
100 μm
Pv
olivine
Pyx
Sp
Sp-Pv-Pyx

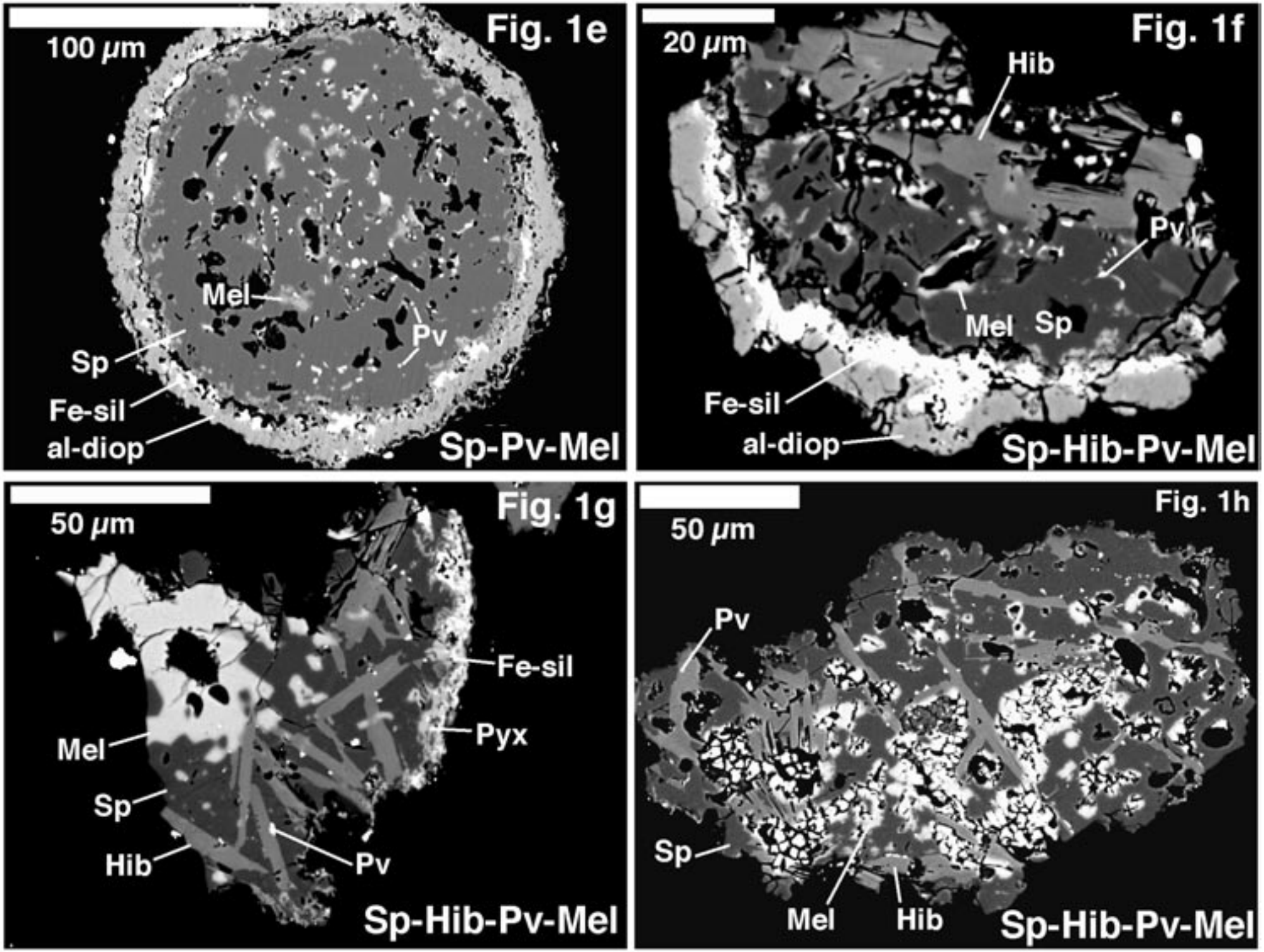
Fig. 1e
100 μm
Mel
Pv
Sp
Fe-sil
al-diop
Sp-Pv-Mel
Fig. 1f
20 μm
Hib
Pv
Mel
Sp
Fe-sil
al-diop
Sp-Hib-Pv-Mel
Fig. 1g
50 μm
Fe-sil
Pyx
Mel
Sp
Hib
Pv
Sp-Hib-Pv-Mel
Fig. 1h
50 μm
Pv
Sp
Mel
Hib
Sp-Hib-Pv-Mel

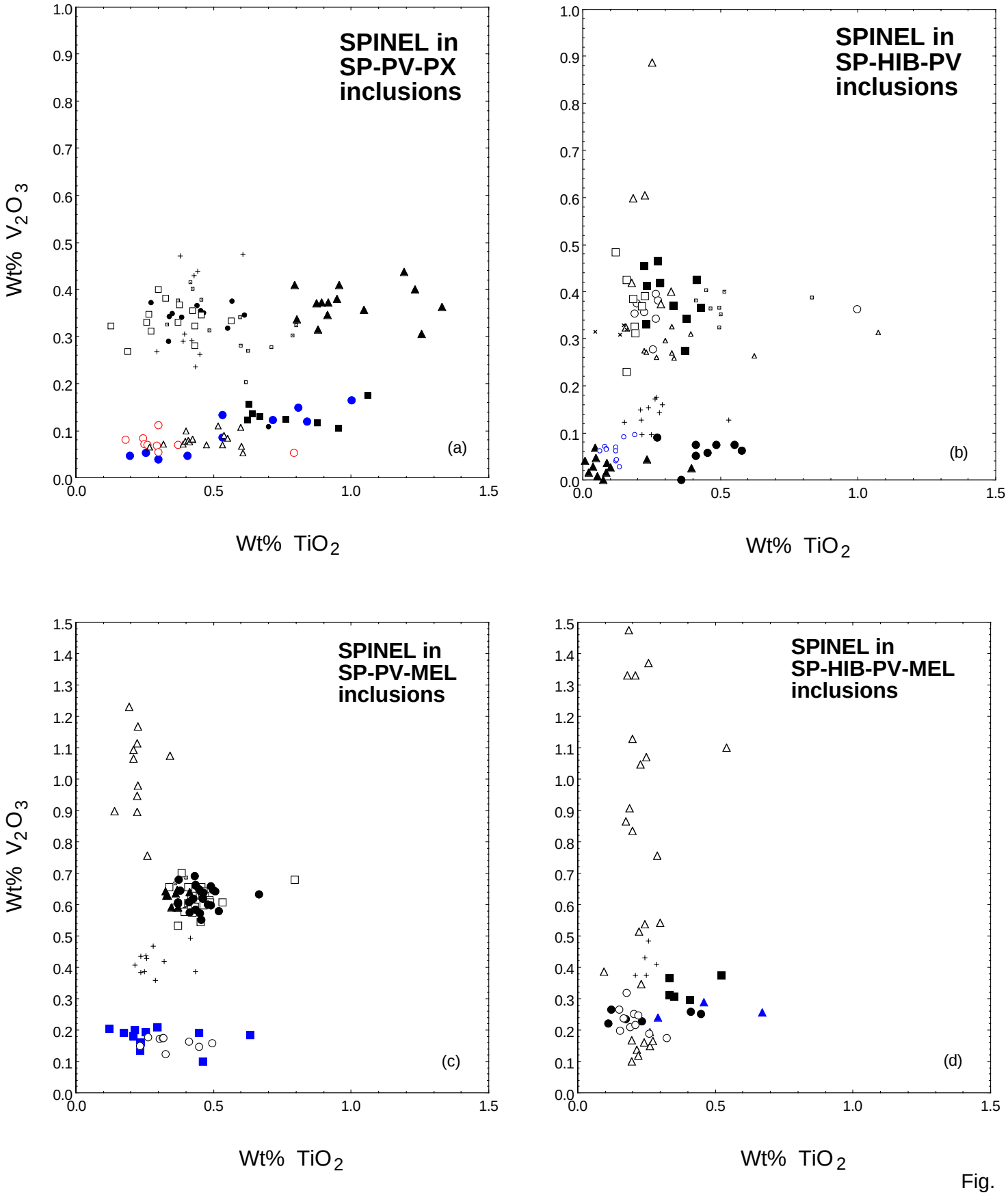
SPINEL in SP-PV-PX inclusions
(a)
SPINEL in SP-HIB-PV inclusions
(b)
SPINEL in SP-PV-MEL inclusions
(c)
SPINEL in SP-HIB-PV-MEL inclusions
(d)
Wt% V2O3
Wt% TiO2
0.0
0.5
1.0
1.5

Fig. 2

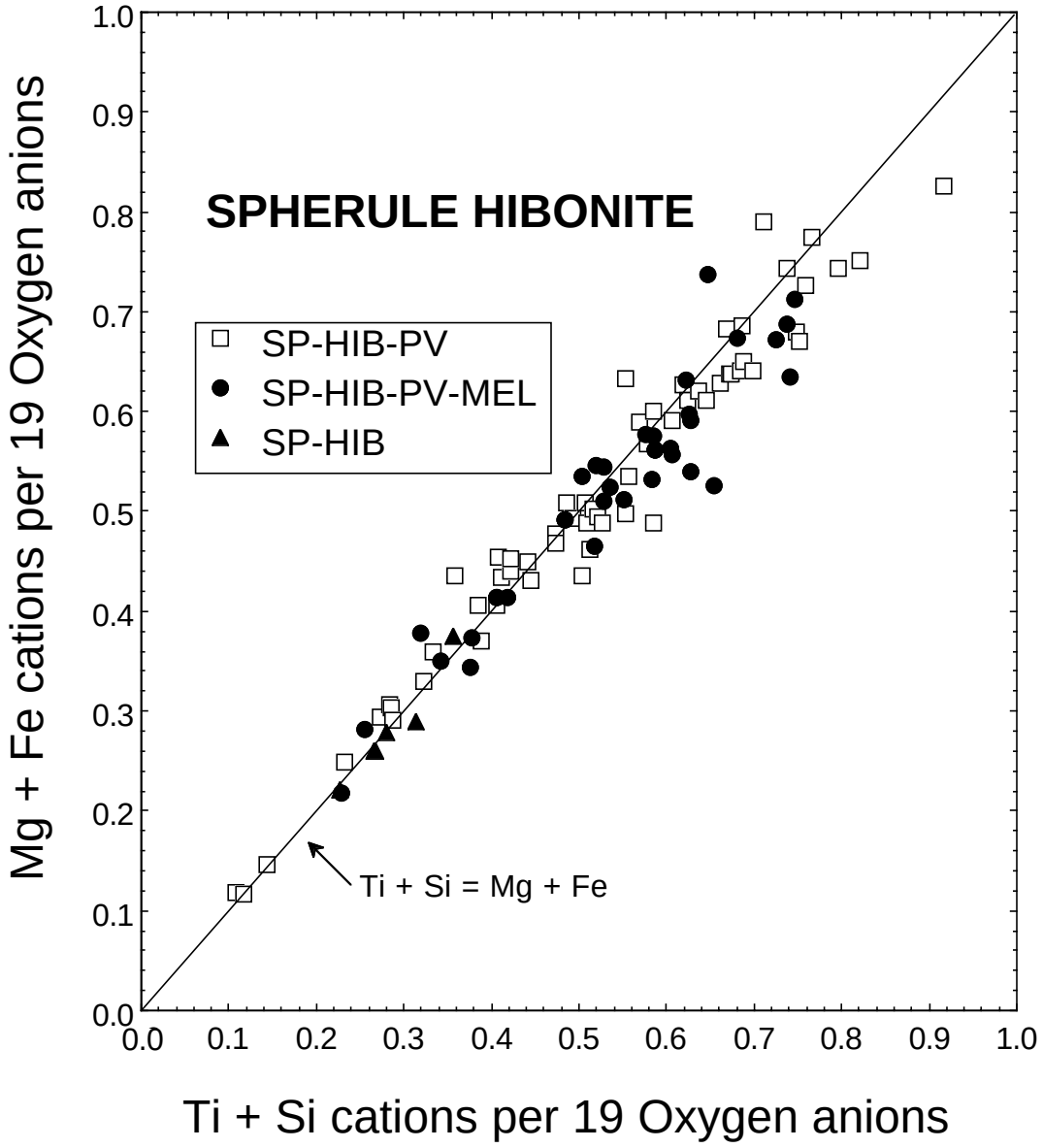
SPHERULE HIBONITE
SP-HIB-PV
SP-HIB-PV-MEL
SP-HIB
Ti + Si = Mg + Fe
Mg + Fe cations per 19 Oxygen anions
Ti + Si cations per 19 Oxygen anions
0.0
0.1
0.2
0.3
0.4
0.5
0.6
0.7
0.8
0.9
1.0

Fig. 3

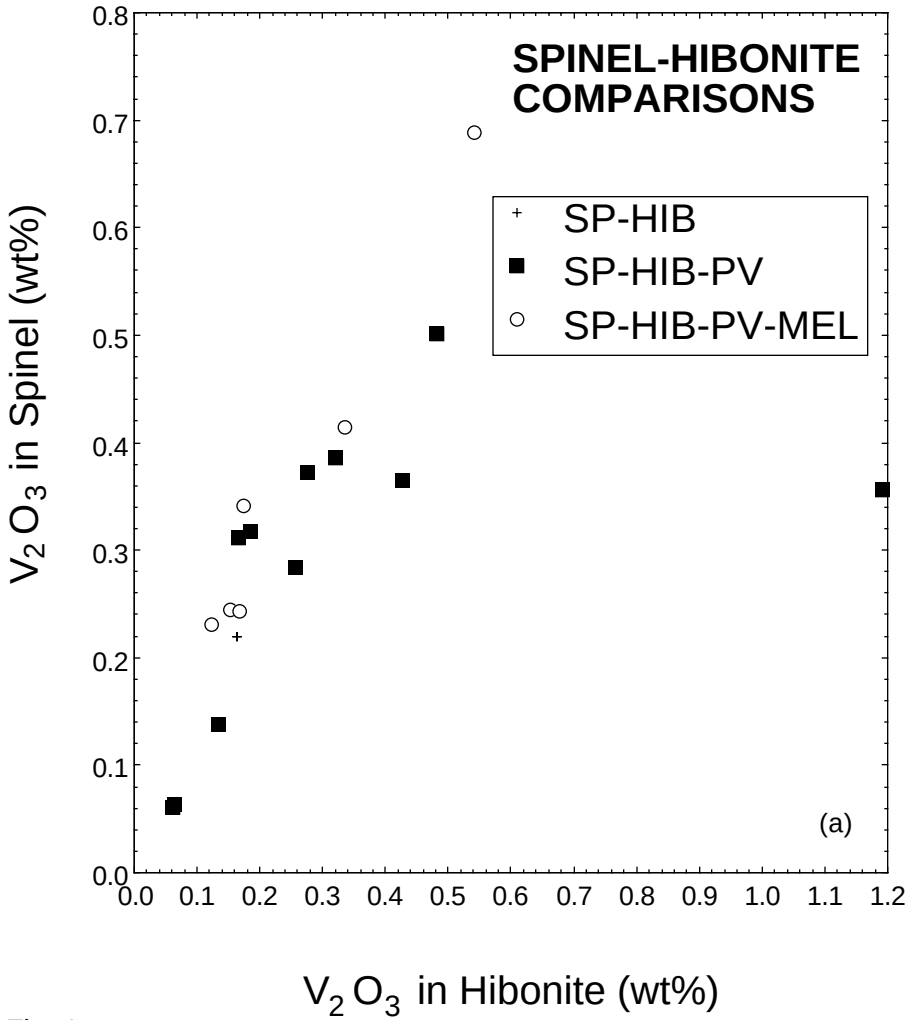
SPINEL-HIBONITE
COMPARISONS
SP-HIB
SP-HIB-PV
SP-HIB-PV-MEL
(a)
V_2O_3 in Spinel (wt%)
V_2O_3 in Hibonite (wt%)
0.0 0.1 0.2 0.3 0.4 0.5 0.6 0.7 0.8
0.0 0.1 0.2 0.3 0.4 0.5 0.6 0.7 0.8 0.9 1.0 1.1 1.2

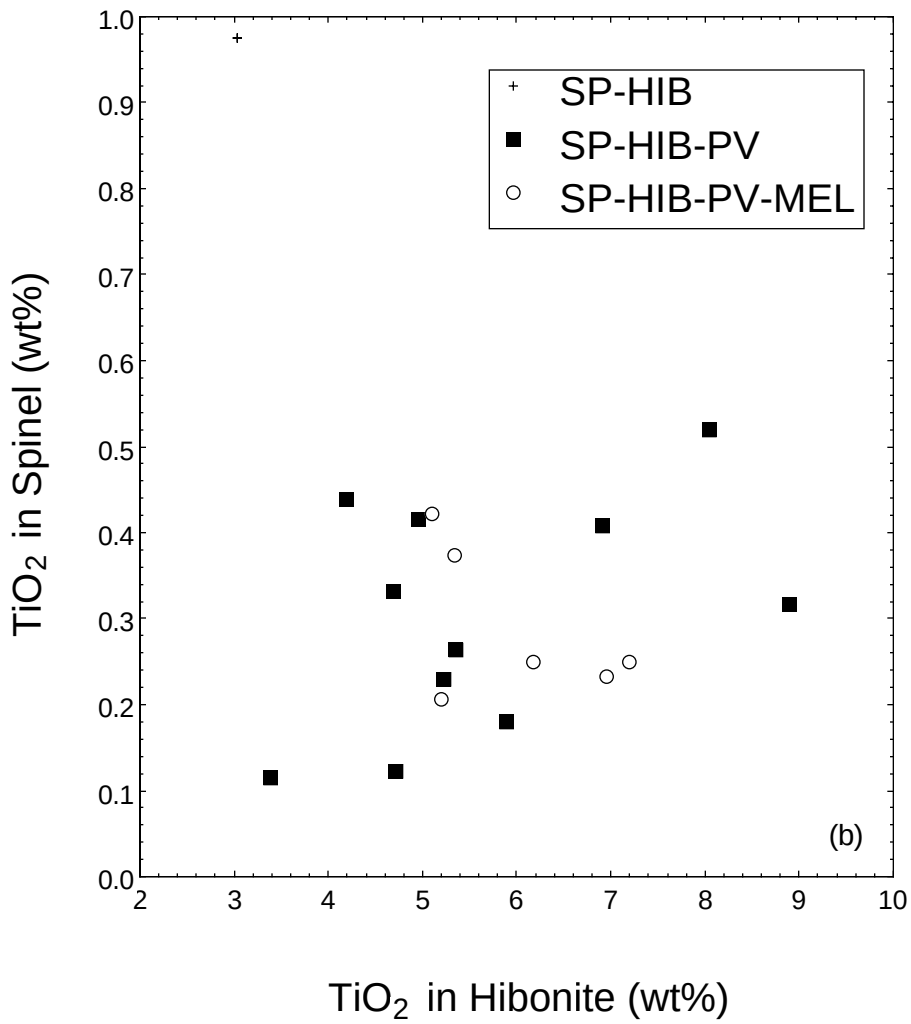
SP-HIB
SP-HIB-PV
SP-HIB-PV-MEL
(b)
TiO_2 in Spinel (wt%)
TiO_2 in Hibonite (wt%)
0.0 0.1 0.2 0.3 0.4 0.5 0.6 0.7 0.8 0.9 1.0
2 3 4 5 6 7 8 9 10

Fig. 4

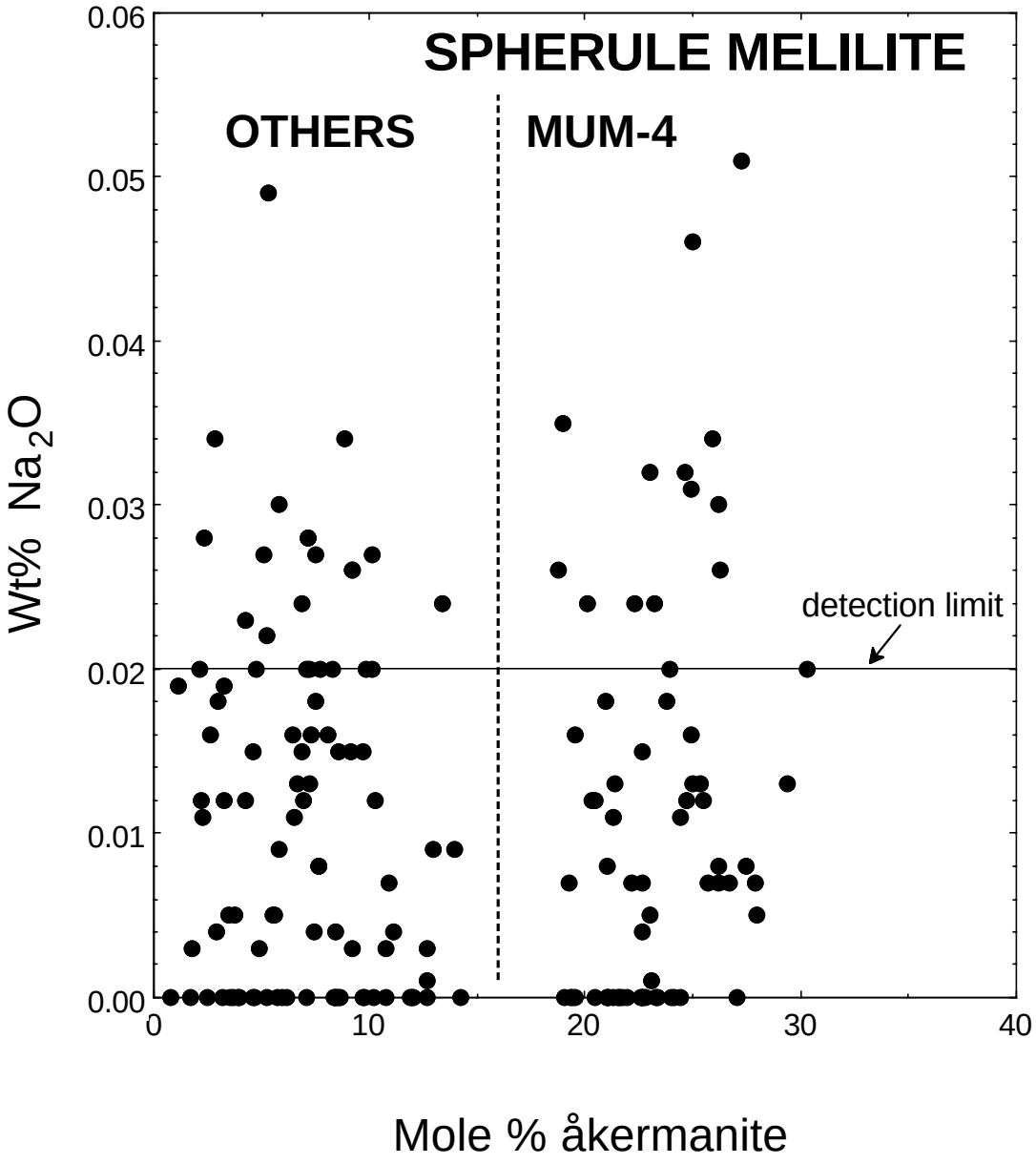
SPHERULE MELILITE
OTHERS
MUM-4
detection limit
Wt% Na2O
Mole % åkermanite
0.06
0.05
0.04
0.03
0.02
0.01
0.00
0
10
20
30
40

Fig. 5

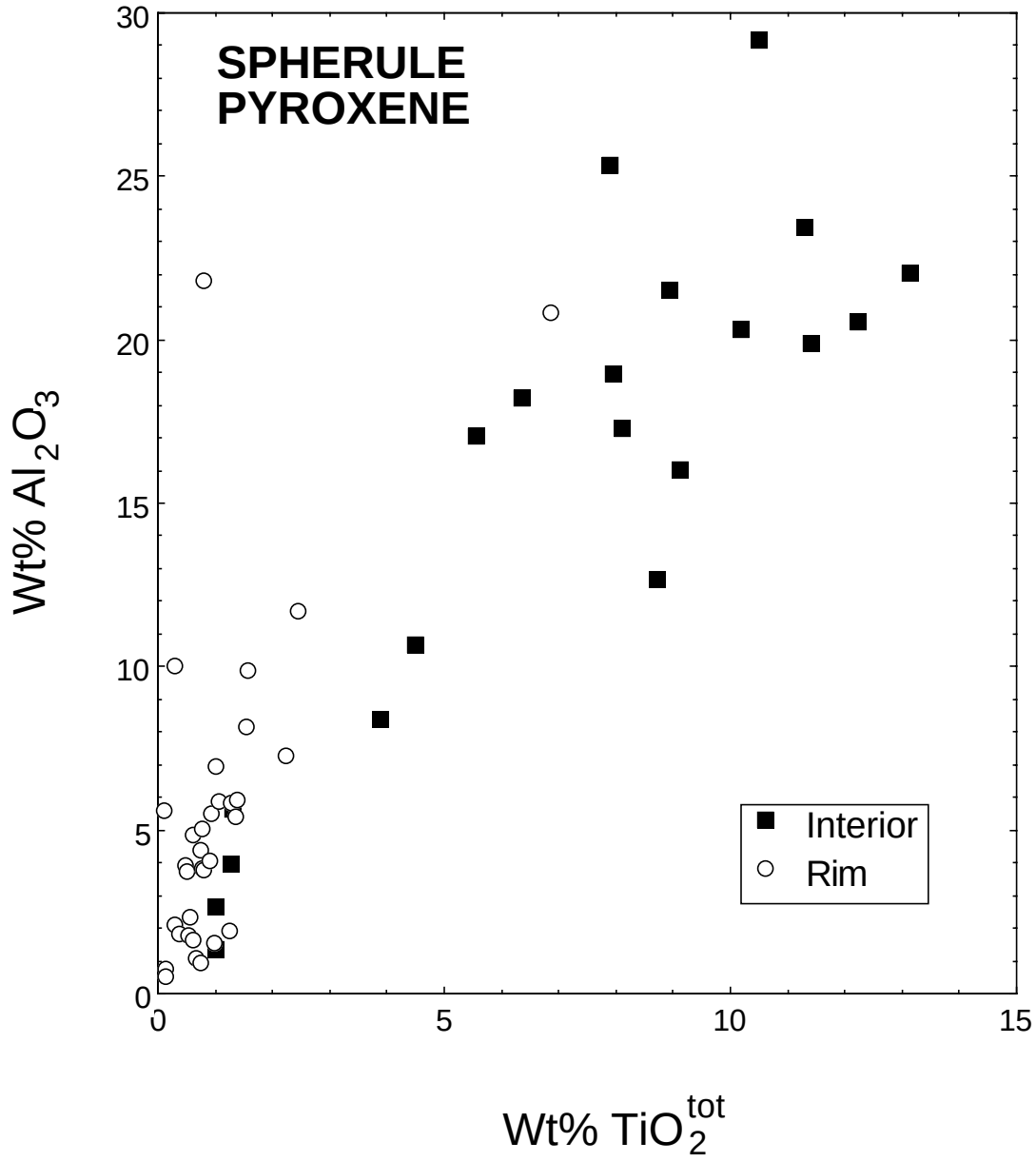
SPHERULE
PYROXENE
Interior
Rim
Wt% Al_2O_3
Wt% TiO_2^{tot}
0
5
10
15
20
25
30

Fig. 6

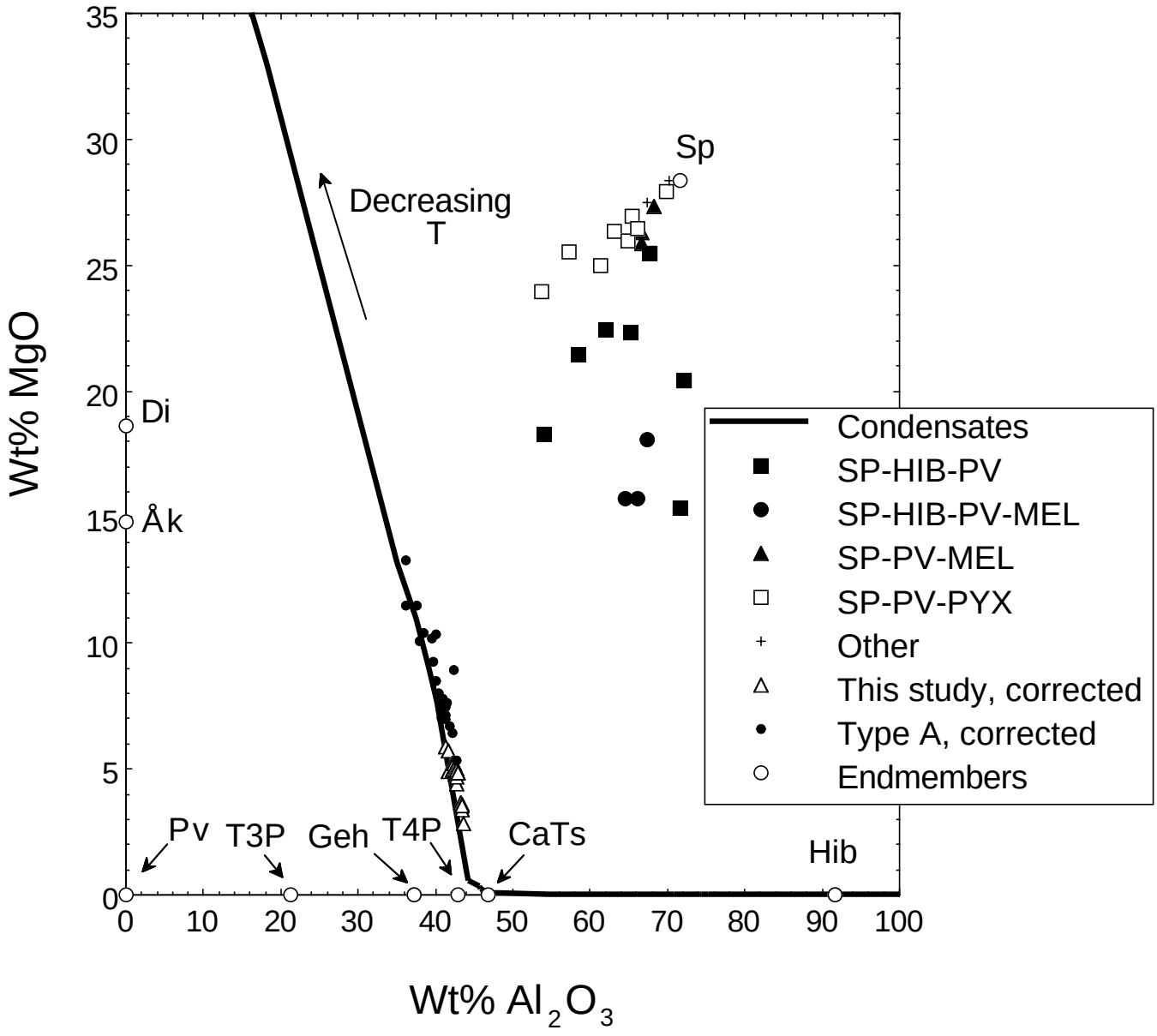
Wt% MgO
Wt% Al2O3
Decreasing T
Sp
Di
Åk
Pv
T3P
Geh
T4P
CaTs
Hib
Condensates
SP-HIB-PV
SP-HIB-PV-MEL
SP-PV-MEL
SP-PV-PYX
Other
This study, corrected
Type A, corrected
Endmembers

Fig. 7

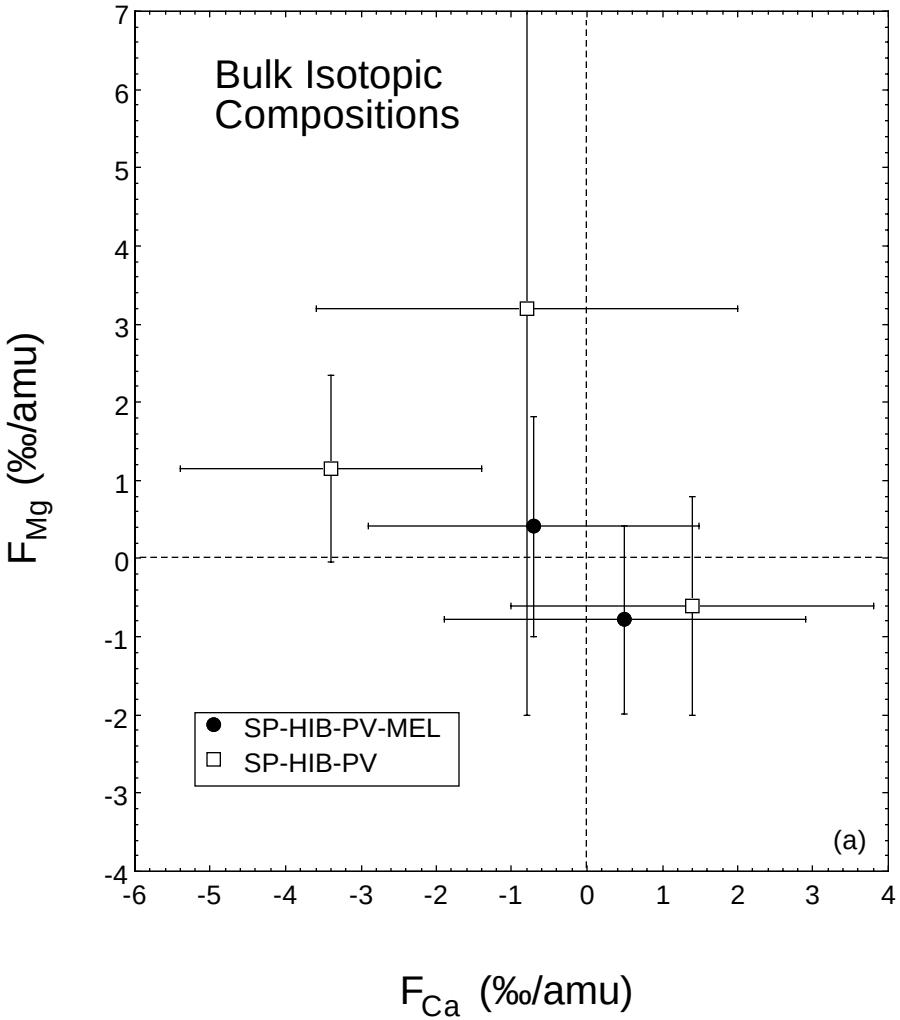
Bulk Isotopic Compositions
SP-HIB-PV-MEL
SP-HIB-PV
(a)
F_Mg (‰/amu)
F_Ca (‰/amu)

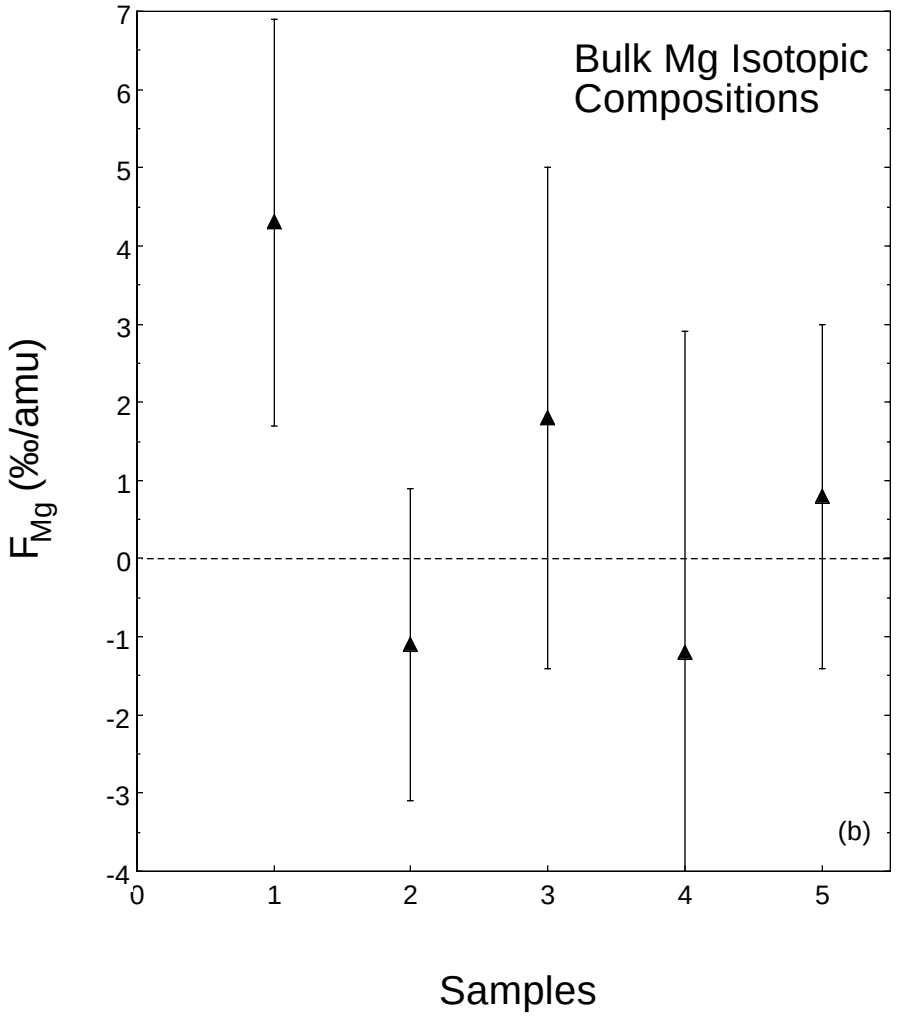
Bulk Mg Isotopic Compositions
(b)
F_Mg (‰/amu)
Samples

Fig. 8

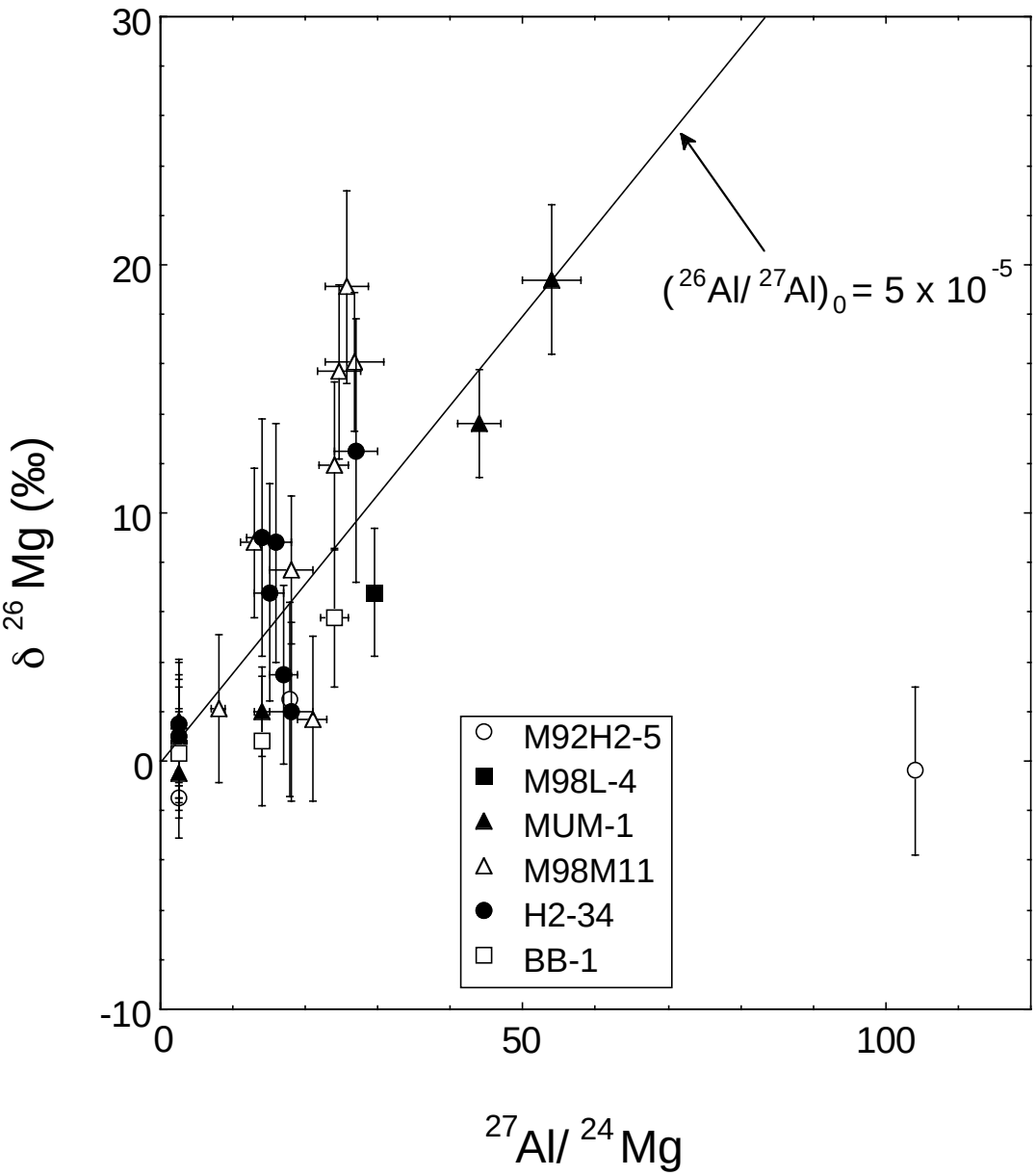
30
20
10
0
-10
0
50
100
δ 26 Mg (‰)
27Al/ 24Mg
(26Al/ 27Al)0 = 5 x 10-5
M92H2-5
M98L-4
MUM-1
M98M11
H2-34
BB-1

Fig. 9

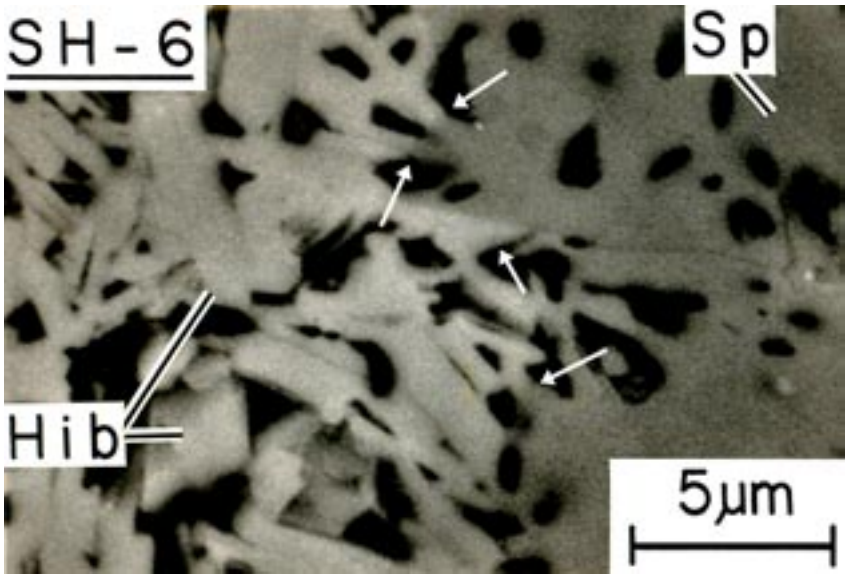
SH-6
Sp
Hib
5μm

Fig. 11

Hibonite ("spinel slab")

(after Wagner and O'Keeffe, 1988)

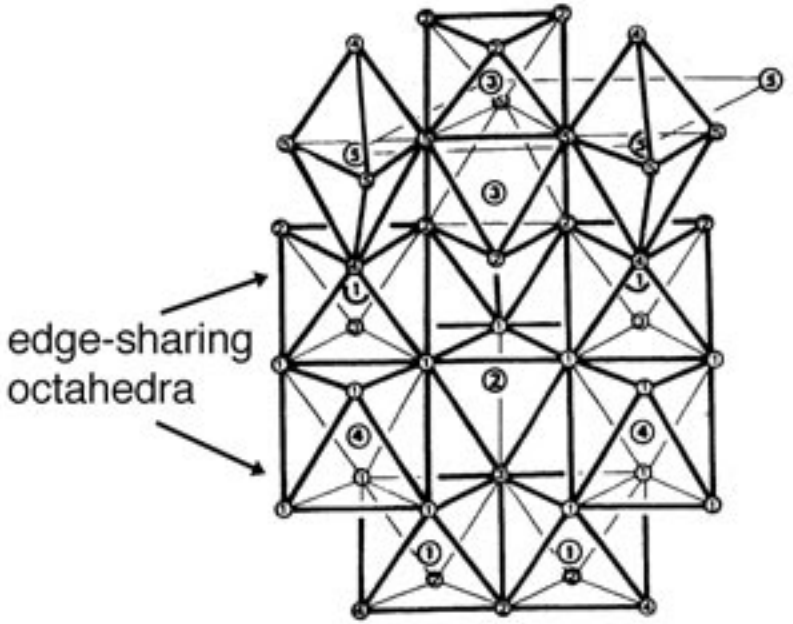

Spinel

(after Waychunas, 1991)

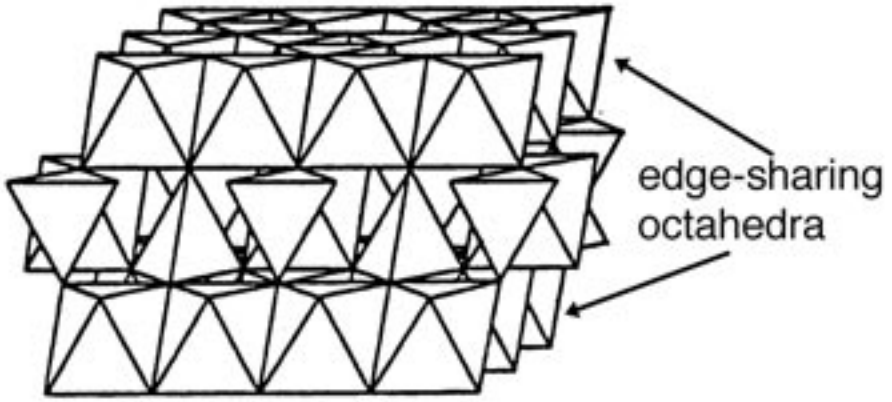

Fig. 12